JOURNAL OF THE AMERICAN CHEMICAL SOCIETY

pubs.acs.org/JACS

Communication

Pore-Space-Partition-Enabled Exceptional Ethane Uptake and Ethane-Selective Ethane–Ethylene Separation

Huajun Yang, Yanxiang Wang, Rajamani Krishna,* Xiaoxia Jia, Yong Wang, Anh N. Hong, Candy Dang, Henry E. Castillo, Xianhui Bu,* and Pingyun Feng*

Cite This: J. Am. Chem. Soc. 2020, 142, 2222–2227

Read Online

ACCESS | Metrics & More | Article Recommendations | Supporting Information

ABSTRACT: An ideal material for C_2H_6/C_2H_4 separation would simultaneously have the highest C_2H_6 uptake capacity and the highest C_2H_6/C_2H_4 selectivity. But such material is elusive. A benchmark material for ethane-selective C_2H_6/C_2H_4 separation is peroxo-functionalized MOF-74-Fe that exhibits the best known separation performance due to its high C_2H_6/C_2H_4 selectivity (4.4), although its C_2H_6 uptake capacity is moderate (74.3 cm^3/g). Here, we report a family of pore-space-partitioned crystalline porous materials (CPMs) with exceptional C_2H_6 uptake capacity and C_2H_6/C_2H_4 separation potential (i.e., C_2H_4 recovered from the mixture) despite their moderate C_2H_6/C_2H_4 selectivity (up to 1.75). The ethane uptake capacity as high as 166.8 cm^3/g at 1 atm and 298 K, more than twice that of peroxo-MOF-74-Fe, has been achieved even though the isosteric heat of adsorption (21.9–30.4 kJ/mol) for these CPMs is as low as about one-third of that for peroxo-MOF-74-Fe (66.8 kJ/mol). While the overall C_2H_6/C_2H_4 separation potentials have not yet surpassed peroxo-MOF-74-Fe, these robust CPMs exhibit outstanding properties including high thermal stability (up to 450 °C) and aqueous stability, low regeneration energy, and a high degree of chemical and geometrical tunability within the same isoreticular framework.

The separation of ethane from ethylene is a vital process in chemical industry and is also energy-intensive.[1] Compared with commonly used cryogenic distillation, adsorptive separation using porous materials would be more energy-efficient.[2,3] Such separation can be performed with either ethane- or ethylene-selective materials,[4−8] but ethane-selective materials enjoy the simplicity of being able to produce ethylene directly at the outlet.[9−13] This work seeks to demonstrate a high-performance platform for ethane-selective alkane/alkene separation.

A chemical separation benefits from both uptake capacity and selectivity and can be most efficiently done with a material that excels in both aspects.[14−19] In practice, however, the interplay between capacity and selectivity makes it hard to maximize both for the same material and a trade-off is often observed.[20] Regarding the aspect of C_2H_6/C_2H_4 selectivity, a breakthrough was recently reported with the synthesis of a peroxo-functionalized MOF-74-Fe ($Fe_2(O_2)$dobdc, denoted here peroxo-MOF-74-Fe) with the highest known C_2H_6/C_2H_4 selectivity, leading to the best reported separation performance despite its relatively low ethane uptake (74.3 cm^3/g).[12,21,22] In addition to peroxo-MOF-74-Fe, a few other materials have also been reported to have high C_2H_6/C_2H_4 selectivity (>2),[10,11] but for these materials, both metrics (selectivity and ethane uptake) are well below that of peroxo-MOF-74-Fe, which significantly widens the gap between their separation performance and that of peroxo-MOF-74-Fe. There are also some ethane-selective materials with C_2H_6 uptakes greater than that of peroxo-MOF-74-Fe (e.g., 116.7 cm^3/g for PCN-250), which helps to narrow the gap in separation potential.[23−28]

While the chemical functionalization strategy as shown by peroxo-MOF-74-Fe is effective at tuning host–guest interactions and therefore the C_2H_6/C_2H_4 selectivity, it may at times come with unintended consequences, such as decreased stability. For large-scale gas separation applications, factors such as long-term stability and adsorbent regeneration cost are also important considerations.[29−37]

In this work, we report the first application of our pore-space-partition (PSP) strategy,[38] a geometry-focused method, for the C_2H_6-selective C_2H_6/C_2H_4 separation. An outstanding feature of this PSP method is that it can dramatically increase the uptake capacity of C_2H_6 to more than 2-fold of the benchmark material peroxo-MOF-74-Fe, and yet the binding strength is just a fraction of that of peroxo-MOF-74-Fe. We show that the C_2H_6/C_2H_4 separation performance can be tuned via any one of three structural modules. Importantly, these materials are highly stable and are capable of excellent ethane-selective C_2H_6/C_2H_4 separation potential due to the ultrahigh C_2H_6 uptake capacity.

The family of materials is built via introduction of a pore-partitioning agent into the hexagonal channel of the MIL-88/MOF-235-type (the **acs** net) framework,[39−41] resulting in the partitioned **acs** net known as the ***pacs*** net.[42,43] They have a general framework formula of [(**M1**$_2$**M2**)(O/OH)**L1**$_3$]**L2**, where **M1** and **M2** are the metals in the trimer, **L1** is the dicarboxylate ligand for the formation of the **acs** framework, and **L2** is the pore-partitioning agent. All the structural

Received: December 6, 2019
Published: January 27, 2020

https://dx.doi.org/10.1021/jacs.9b12924
J. Am. Chem. Soc. 2020, 142, 2222–2227

modules (i.e., **L1**, **L2**, and metal trimers) are tunable with many possibilities. In this work, we have examined the effects of all three modules. The variation in each module is chosen as follows: (Module 1) dicarboxylate ligands - bdc, dmbdc, and ndc; (Module 2) pore-partitioning agent - tpbz, tppy, and tpt; and (Module 3) metal trimers - Co_2V, Co_2Ti, Mg_2V, and Mg_2Ti (Figure 1). While there are 36 permutations by combining these modules, we are able to establish general trends in ethane-selective C_2H_6/C_2H_4 separation properties with nine combinations reported here.

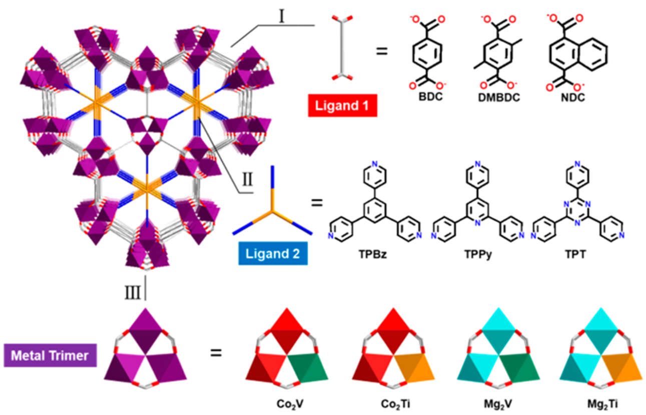

Figure 1. Three modules of *pacs* MOFs studied in this work. Three kinds of Ligand Type 1, three kinds of Ligand Type 2 and four kinds of metal trimers are used (BDC = terephthalate; DMBDC = 2,5-dimethylterephthalate; NDC = 1,4-naphthalenedicarboxylate; TPBz = 1,3,5-tri(4-pyridyl)-benzene, TPPy = 2,4,6-tris(4-pyridyl)pyridine, TPT = 2,4,6-tri(4-pyridyl)-1,3,5-triazine).

The metal combinations such as Co−V trimers in this study are unusual among MOFs. The heterometallic compositions were established by EDS analysis (Figure S2) and supported by single-crystal X-ray diffraction analysis. It is worth noting that while it is typically difficult to grow large single crystals of vanadium and titanium MOFs for use with a conventional X-ray source, crystals around 50 μm in size can be made readily in this work,[44−47] and seven structures reported here were analyzed with in-house single-crystal diffraction data.

The materials in this work are highly stable. They are thermally stable up to 450 °C (Figures S3−S4). All of them maintain their structural integrity after repeated gas adsorption−desorption experiments (Figure S5). As shown by Figure S6, Co_2Ti-bdc-tpt and Co_2V-bdc-tpt are hydrothermally stable and could retain their high crystallinity even after immersion in water for 24 h.

In addition to partitioning the pore space, pore-partitioning agents deactivate all open-metal sites (OMS) of the parent 6-connected **acs** framework. While OMSs can be beneficial for ethylene-selective C_2H_4/C_2H_6 separation,[4] the total annihilation of OMS in this family of materials could be helpful for ethane-selective C_2H_4/C_2H_6 separation. In fact, all the MOFs in this work show ethane-selective C_2H_4/C_2H_6 separation according to the single-component adsorption isotherms (Figures S7−S15). Moreover, the ethane uptakes of these MOFs are remarkably high. Six of nine MOFs have the uptake capacity from 154.2 to 166.8 cm^3/g at 298 K and 1 atm (Table S2), all of which by far exceed 116.7 cm^3/g for PCN-250, a benchmark material for ethane uptake among ethane-selective MOFs. This corresponds to about 6−7 C_2H_6 molecules per formula unit. In particular, the uptake by Mg_2V-bdc-tpt is 166.8 cm^3/g (7.45 mmol/g), which is likely the highest among MOFs reported to date (Figure 2 and Tables S3−S4).

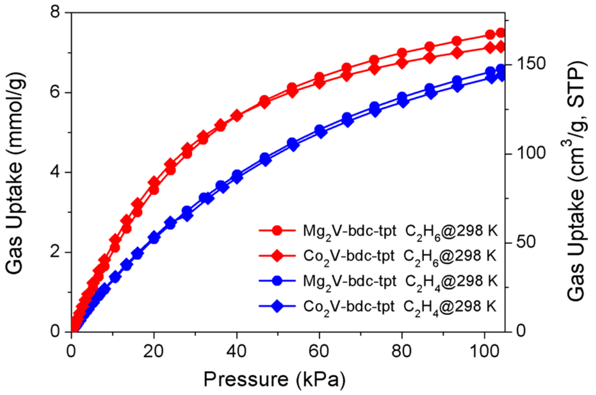

Figure 2. Experimental C_2H_6 and C_2H_4 adsorption isotherms of Mg_2V-bdc-tpt and Co_2V-bdc-tpt at 298 K.

The high ethane uptakes are accomplished with low adsorption enthalpies ranging from 21.9 to 30.4 kJ/mol at zero coverage (Figure S16). In contrast, $Fe_2(O_2)$(dobdc) has a high ethane adsorption enthalpy (66.8 kJ/mol).[12] The low Q_{st} of CPMs could be advantageous for adsorbent regeneration due to the reduced energy consumption. The low adsorption enthalpy was further validated by GCMC simulations. The density distribution of C_2H_6 molecules within Co_2V-bdc-tpt was analyzed at different pressures (Figure S17). No strong adsorption sites were observed on the framework. Also, the density distribution of C_2H_6 molecules was found to be quite dispersive in all the pore space, indicative of the widespread weak adsorption sites that are responsible for the ultrahigh C_2H_6 uptake.

The IAST selectivity has been calculated to evaluate the separation performance (Figure S18). The best selectivity is 1.75 for Co_2V-bdc-tpt, which is comparable to ZIF-7 (1.5), IRMOF-8 (1.6), PCN-250 (1.9), and MUF-15 (1.96), but significantly lower than $Fe_2(O_2)$(dobdc) (4.4), $Cu(Qc)_2$ (3.4), and MAF-49 (2.7) (Table S3).

In addition to uptake capacity and selectivity, separation potential, which is a metric incorporating the influence of both factors, is also used to evaluate the separation performance.[48,49] It represents the maximum amount of pure C_2H_4 that could be recovered from the mixture in a fixed bed adsorber; the separation potentials are calculable from IAST using eq S3 in the SI. Separation potentials, together with the uptake capacity and selectivity of nine materials, are discussed below when we systematically vary one structural module while keeping two other modules unchanged.

As shown in Figure 3a, the BDC ligand was determined to have the best separation potential. We explored the possibility of boosting C_2H_6 uptake by incorporating nonpolar groups which was considered helpful in some structure types studied previously.[50,51] It was observed here that nonpolar functionalization on dicarboxylate ligands does not improve separation performance. An increase in C_2H_6 adsorption enthalpy was indeed observed with the installation of nonpolar groups in the Co_2V compositions from 23.4 for Co_2V-bdc-tpt to 27.9 for Co_2V-dmbdc-tpt and to 30.4 kJ/mol for Co_2V-ndc-tpt (Figure S15). However, the extra group also led to a significant decrease in surface area (Figure S19), which likely resulted in a significant decrease in C_2H_6 uptake capacity. The BET surface

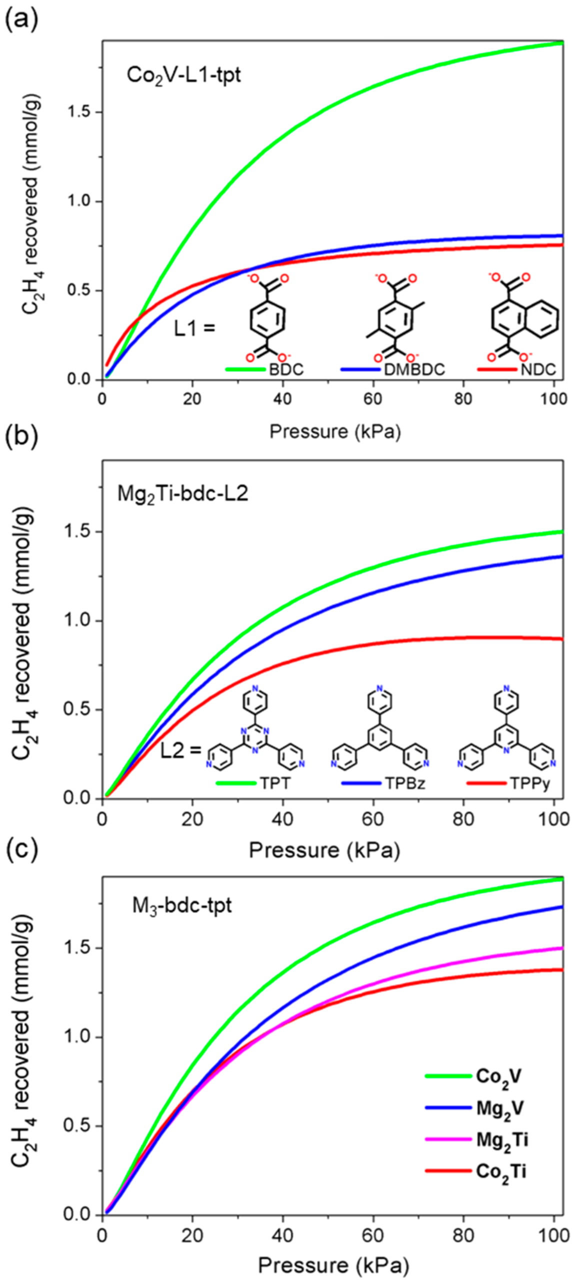

Figure 3. Comparisons of separation potential for C_2H_6/C_2H_4 (50/50) mixture: (a) Co_2V-L1-tpt with different dicarboxylate ligands; (b) Mg_2Ti-bdc-L2 with different pore-partitioning agents; (c) M_3-bdc-tpt with different metal trimers.

areas decreased from 1328.5 m^2/g for Co_2V-bdc-tpt to 1161.5 m^2/g for Co_2V-dmbdc-tpt and to 472.5 m^2/g for Co_2V-ndc-tpt. Following the same trend, the C_2H_6 uptake decreased from 159.6 cm^3/g for Co_2V-bdc-tpt to 104.6 cm^3/g for Co_2V-dmbdc-tpt and to 90.2 cm^3/g for Co_2V-ndc-tpt (Table S2). Furthermore, the Co_2V-bdc-tpt also has the highest C_2H_6/C_2H_4 selectivity among all the phases reported here (Figure S18). For the Mg_2V system, Mg_2V-bdc-tpt also outperforms Mg_2V-dmbdc-tpt in terms of uptake capacity and selectivity (Figure S21).

In comparison with the module 1 (dicarboxylates) that exhibits a large impact on C_2H_6/C_2H_4 uptake capacity, the module 2 (pore-partitioning agent) exerts a significant impact on C_2H_6/C_2H_4 selectivity. Overall, the separation potential for this family of MOFs with a different pore-partitioning agent follows the order of tpt > tpbz > tppy (Figure 3b). These materials (Mg_2Ti-bdc-tpbz, Mg_2Ti-bdc-tppy, and Mg_2Ti-bdc-tpt) have similar surface areas and ethane uptakes, but their selectivity differs obviously. The lowest selectivity for ethane was found in Mg_2Ti-bdc-tppy (Figure S18), which led to its lowest separation potential. This may be due to the more basic feature of the pyridine core in the partitioning agent (as compared to the cores in tpt and tpbz), which enables a relatively stronger interaction with ethylene.

With bdc and tpt as the best choices for C_2H_6/C_2H_4 separation, the effects of metal trimers on the separation potential were subsequently evaluated. The order was found to be Co_2V > Mg_2V > Mg_2Ti > Co_2Ti (Figure 3c). The best performance of Co_2V-bdc-tpt among this family is due to the combined effect from uptake capacity and selectivity (Table S2). Also, vanadium MOFs show higher separation performance than titanium MOFs with the same **M1** (Co or Mg).

Co_2V-bdc-tpt and Mg_2V-bdc-tpt could produce 1.88 and 1.73 mmol/g C_2H_4 from the C_2H_6/C_2H_4 (50/50) mixture, respectively. These values are lower than that of Fe_2O_2(dobdc) (1.93), but higher than those of other prominent MOFs (Figure 4a). Other materials reported here such as Mg_2Ti-bdc-tpt and Co_2Ti-bdc-tpt also show high separation potentials.

To validate the excellent separation performance, transient breakthrough simulations were also performed using Co_2V-

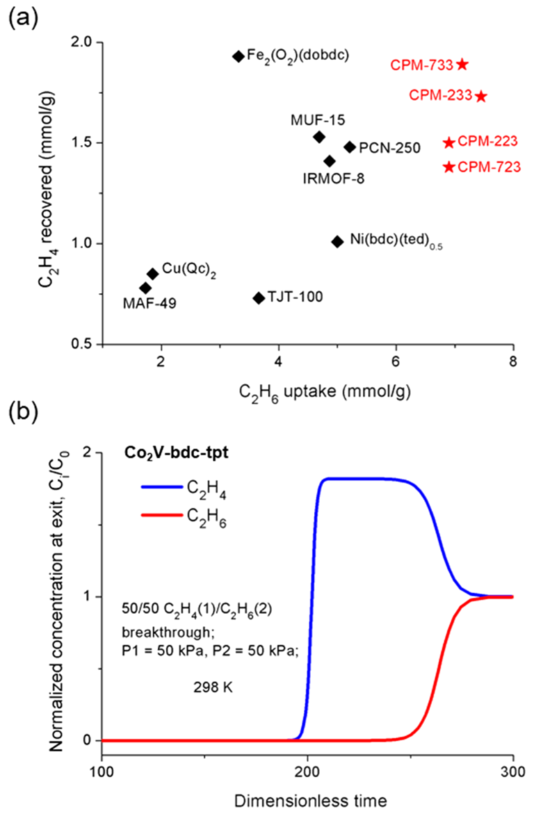

Figure 4. (a) Separation potential (calculated using eq S3 of the SI) versus single-component ethane uptake for the select high-performance ethane-selective materials reported to date (CPM-733: Co_2V-bdc-tpt; CPM-233: Mg_2V-bdc-tpt; CPM-223: Mg_2Ti-bdc-tpt; CPM-723: Co_2Ti-bdc-tpt). (b) Simulated breakthrough curve for CPM-733. Binary equimolar C_2H_6/C_2H_4 mixtures were used in all calculations and simulations.

https://dx.doi.org/10.1021/jacs.9b12924
J. Am. Chem. Soc. 2020, 142, 2222−2227

bdc-tpt and Mg_2V-bdc-tpt. C_2H_6/C_2H_4 mixtures with two ratios (50/50 and 10/90) were used as feeding gases in the simulation to mimic the industrial separation process. The results clearly show that both materials are capable of separating these two gases. In the simulated breakthrough curves, the C_2H_4 breakthrough occurred first and subsequently reached a plateau, which could thereby produce polymer-grade C_2H_4 before the C_2H_6 breakthrough occurred (Figure 4b). The productivities were also calculated based on the breakthrough curves. For the 50/50 C_2H_6/C_2H_4 mixture, Co_2V-bdc-tpt and Mg_2V-bdc-tpt can produce 0.88 and 0.60 mmol/g C_2H_4 (purity >99.95%), respectively. These values are higher than some benchmark MOFs including MAF-49 (0.52 mmol/g), and $Cu(Qc)_2$ (0.49 mmol/g). Similarly, excellent separation performances were also found in Co_2V-bdc-tpt and Mg_2V-bdc-tpt with the 10/90 C_2H_6/C_2H_4 mixture (Figure S22).

In conclusion, we have made nine heterometallic vanadium and titanium MOFs and systematically investigated the effects of three separate modules on the C_2H_6/C_2H_4 separation performance. Compared with Fe_2O_2(dobdc) with very high selectivity, this family of materials have exceptional high uptake and provide an alternative way to achieve excellent separation performance. Some advantages of this family of materials include high stability, easy adsorbent regeneration, and broad chemical tunability. The correlations between the structure and the C_2H_6/C_2H_4 separation performance revealed in this work could be useful for designing novel high-performance C_2H_6-selective MOFs. Finally, novel metal combinations in this work highlight new possibilities for the construction of trimer-based MOFs.

■ ASSOCIATED CONTENT

Supporting Information

The Supporting Information is available free of charge at https://pubs.acs.org/doi/10.1021/jacs.9b12924.

Experimental Procedures and compound characterization data (PDF)

Crystallographic data with CCDC Nos. 1967756–1967761 (CIF)

■ AUTHOR INFORMATION

Corresponding Authors

Rajamani Krishna – *Van't Hoff Institute for Molecular Sciences, University of Amsterdam, 1098 XH Amsterdam, The Netherlands;* orcid.org/0000-0002-4784-8530; Email: r.krishna@contact.uva.nl

Xianhui Bu – *Department of Chemistry and Biochemistry, California State University, Long Beach, California 90840, United States;* orcid.org/0000-0002-2994-4051; Email: xianhui.bu@csulb.edu

Pingyun Feng – *Department of Chemistry, University of California, Riverside, California 92521, United States;* orcid.org/0000-0003-3684-577X; Email: pingyun.feng@ucr.edu

Authors

Huajun Yang – *Department of Chemistry and Biochemistry, California State University, Long Beach, California 90840, United States; Department of Chemistry, University of California, Riverside, California 92521, United States;* orcid.org/0000-0002-4664-4042

Yanxiang Wang – *Department of Chemistry, University of California, Riverside, California 92521, United States*

Xiaoxia Jia – *Department of Chemistry, University of California, Riverside, California 92521, United States*

Yong Wang – *Department of Chemistry, University of California, Riverside, California 92521, United States;* orcid.org/0000-0002-8002-4840

Anh N. Hong – *Department of Chemistry, University of California, Riverside, California 92521, United States;* orcid.org/0000-0003-1808-5527

Candy Dang – *Department of Chemistry and Biochemistry, California State University, Long Beach, California 90840, United States*

Henry E. Castillo – *Department of Chemistry and Biochemistry, California State University, Long Beach, California 90840, United States*

Complete contact information is available at: https://pubs.acs.org/10.1021/jacs.9b12924

Notes

The authors declare no competing financial interest.

■ ACKNOWLEDGMENTS

The thermal stability and ethane-ethylene gas sorption and separation studies are supported by the US Department of Energy, Office of Basic Energy Sciences, Materials Sciences and Engineering Division under Award No. DE-SC0010596 (P.F.). The synthesis and X-ray diffraction studies are supported by NSF-DMR, under Award No. 1708850 (X.B.).

■ REFERENCES

(1) Ren, T.; Patel, M.; Blok, K. Olefins from conventional and heavy feedstocks: Energy use in steam cracking and alternative processes. *Energy* **2006**, *31*, 425.

(2) Sholl, D. S.; Lively, R. P. Seven chemical separations to change the world. *Nature* **2016**, *532*, 435.

(3) Li, J.-R.; Sculley, J.; Zhou, H.-C. Metal–Organic Frameworks for Separations. *Chem. Rev.* **2012**, *112*, 869.

(4) Bloch, E. D.; Queen, W. L.; Krishna, R.; Zadrozny, J. M.; Brown, C. M.; Long, J. R. Hydrocarbon Separations in a Metal-Organic Framework with Open Iron(II) Coordination Sites. *Science* **2012**, *335*, 1606.

(5) Lin, R.-B.; Li, L.; Zhou, H.-L.; Wu, H.; He, C.; Li, S.; Krishna, R.; Li, J.; Zhou, W.; Chen, B. Molecular sieving of ethylene from ethane using a rigid metal–organic framework. *Nat. Mater.* **2018**, *17*, 1128.

(6) Li, B.; Zhang, Y.; Krishna, R.; Yao, K.; Han, Y.; Wu, Z.; Ma, D.; Shi, Z.; Pham, T.; Space, B.; Liu, J.; Thallapally, P. K.; Liu, J.; Chrzanowski, M.; Ma, S. Introduction of π-Complexation into Porous Aromatic Framework for Highly Selective Adsorption of Ethylene over Ethane. *J. Am. Chem. Soc.* **2014**, *136*, 8654.

(7) He, Y.; Krishna, R.; Chen, B. Metal–organic frameworks with potential for energy-efficient adsorptive separation of light hydrocarbons. *Energy Environ. Sci.* **2012**, *5*, 9107.

(8) Yang, S.; Ramirez-Cuesta, A. J.; Newby, R.; Garcia-Sakai, V.; Manuel, P.; Callear, S. K.; Campbell, S. I.; Tang, C. C.; Schröder, M. Supramolecular binding and separation of hydrocarbons within a functionalized porous metal–organic framework. *Nat. Chem.* **2015**, *7*, 121.

(9) Gücüyener, C.; van den Bergh, J.; Gascon, J.; Kapteijn, F. Ethane/Ethene Separation Turned on Its Head: Selective Ethane Adsorption on the Metal-Organic Framework ZIF-7 through a Gate-Opening Mechanism. *J. Am. Chem. Soc.* **2010**, *132*, 17704.

(10) Liao, P.-Q.; Zhang, W.-X.; Zhang, J.-P.; Chen, X.-M. Efficient purification of ethene by an ethane-trapping metal-organic framework. *Nat. Commun.* **2015**, *6*, 8697.

(11) Lin, R.-B.; Wu, H.; Li, L.; Tang, X.-L.; Li, Z.; Gao, J.; Cui, H.; Zhou, W.; Chen, B. Boosting Ethane/Ethylene Separation within Isoreticular Ultramicroporous Metal−Organic Frameworks. *J. Am. Chem. Soc.* **2018**, *140*, 12940.

(12) Li, L.; Lin, R.-B.; Krishna, R.; Li, H.; Xiang, S.; Wu, H.; Li, J.; Zhou, W.; Chen, B. Ethane/ethylene separation in a metal-organic framework with iron-peroxo sites. *Science* **2018**, *362*, 443.

(13) Chen, K.-J.; Madden, D. G.; Mukherjee, S.; Pham, T.; Forrest, K. A.; Kumar, A.; Space, B.; Kong, J.; Zhang, Q.-Y.; Zaworotko, M. J. Synergistic sorbent separation for one-step ethylene purification from a four-component mixture. *Science* **2019**, *366*, 241.

(14) Matsuda, R.; Kitaura, R.; Kitagawa, S.; Kubota, Y.; Belosludov, R. V.; Kobayashi, T. C.; Sakamoto, H.; Chiba, T.; Takata, M.; Kawazoe, Y.; Mita, Y. Highly controlled acetylene accommodation in a metal−organic microporous material. *Nature* **2005**, *436*, 238.

(15) Nguyen, N. T. T.; Furukawa, H.; Gándara, F.; Nguyen, H. T.; Cordova, K. E.; Yaghi, O. M. Selective Capture of Carbon Dioxide under Humid Conditions by Hydrophobic Chabazite-Type Zeolitic Imidazolate Frameworks. *Angew. Chem., Int. Ed.* **2014**, *53*, 10645.

(16) Nugent, P.; Belmabkhout, Y.; Burd, S. D.; Cairns, A. J.; Luebke, R.; Forrest, K.; Pham, T.; Ma, S.; Space, B.; Wojtas, L.; Eddaoudi, M.; Zaworotko, M. J. Porous materials with optimal adsorption thermodynamics and kinetics for CO_2 separation. *Nature* **2013**, *495*, 80.

(17) Cui, X.; Chen, K.; Xing, H.; Yang, Q.; Krishna, R.; Bao, Z.; Wu, H.; Zhou, W.; Dong, X.; Han, Y.; Li, B.; Ren, Q.; Zaworotko, M. J.; Chen, B. Pore chemistry and size control in hybrid porous materials for acetylene capture from ethylene. *Science* **2016**, *353*, 141.

(18) Cadiau, A.; Adil, K.; Bhatt, P. M.; Belmabkhout, Y.; Eddaoudi, M. A metal-organic framework−based splitter for separating propylene from propane. *Science* **2016**, *353*, 137.

(19) Wang, H.; Dong, X.; Colombo, V.; Wang, Q.; Liu, Y.; Liu, W.; Wang, X.-L.; Huang, X.-Y.; Proserpio, D. M.; Sironi, A.; Han, Y.; Li, J. Tailor-Made Microporous Metal−Organic Frameworks for the Full Separation of Propane from Propylene Through Selective Size Exclusion. *Adv. Mater.* **2018**, *30*, 1805088.

(20) Lin, J. Y. S. Molecular sieves for gas separation. *Science* **2016**, *353*, 121.

(21) Bloch, E. D.; Murray, L. J.; Queen, W. L.; Chavan, S.; Maximoff, S. N.; Bigi, J. P.; Krishna, R.; Peterson, V. K.; Grandjean, F.; Long, G. J.; Smit, B.; Bordiga, S.; Brown, C. M.; Long, J. R. Selective Binding of O_2 over N_2 in a Redox−Active Metal−Organic Framework with Open Iron(II) Coordination Sites. *J. Am. Chem. Soc.* **2011**, *133*, 14814.

(22) Queen, W. L.; Bloch, E. D.; Brown, C. M.; Hudson, M. R.; Mason, J. A.; Murray, L. J.; Ramirez-Cuesta, A. J.; Peterson, V. K.; Long, J. R. Hydrogen adsorption in the metal−organic frameworks Fe_2(dobdc) and $Fe_2(O_2)$(dobdc). *Dalton Trans.* **2012**, *41*, 4180.

(23) Qazvini, O. T.; Babarao, R.; Shi, Z.-L.; Zhang, Y.-B.; Telfer, S. G. A Robust Ethane-Trapping Metal−Organic Framework with a High Capacity for Ethylene Purification. *J. Am. Chem. Soc.* **2019**, *141*, 5014.

(24) Chen, Y.; Qiao, Z.; Wu, H.; Lv, D.; Shi, R.; Xia, Q.; Zhou, J.; Li, Z. An ethane-trapping MOF PCN-250 for highly selective adsorption of ethane over ethylene. *Chem. Eng. Sci.* **2018**, *175*, 110.

(25) Liang, W.; Xu, F.; Zhou, X.; Xiao, J.; Xia, Q.; Li, Y.; Li, Z. Ethane selective adsorbent Ni(bdc)$(ted)_{0.5}$ with high uptake and its significance in adsorption separation of ethane and ethylene. *Chem. Eng. Sci.* **2016**, *148*, 275.

(26) Pires, J.; Pinto, M. L.; Saini, V. K. Ethane Selective IRMOF-8 and Its Significance in Ethane−Ethylene Separation by Adsorption. *ACS Appl. Mater. Interfaces* **2014**, *6*, 12093.

(27) Hao, H.-G.; Zhao, Y.-F.; Chen, D.-M.; Yu, J.-M.; Tan, K.; Ma, S.; Chabal, Y.; Zhang, Z.-M.; Dou, J.-M.; Xiao, Z.-H.; Day, G.; Zhou, H.-C.; Lu, T.-B. Simultaneous Trapping of C_2H_2 and C_2H_6 from a Ternary Mixture of $C_2H_2/C_2H_4/C_2H_6$ in a Robust Metal−Organic Framework for the Purification of C_2H_4. *Angew. Chem.* **2018**, *130*, 16299.

(28) Chen, Y.; Wu, H.; Lv, D.; Shi, R.; Chen, Y.; Xia, Q.; Li, Z. Highly Adsorptive Separation of Ethane/Ethylene by An Ethane-Selective MOF MIL-142A. *Ind. Eng. Chem. Res.* **2018**, *57*, 4063.

(29) Trickett, C. A.; Helal, A.; Al-Maythalony, B. A.; Yamani, Z. H.; Cordova, K. E.; Yaghi, O. M. The chemistry of metal−organic frameworks for CO_2 capture, regeneration and conversion. *Nat. Rev. Mater.* **2017**, *2*, 17045.

(30) Furukawa, H.; Cordova, K. E.; O'Keeffe, M.; Yaghi, O. M. The Chemistry and Applications of Metal-Organic Frameworks. *Science* **2013**, *341*, 1230444.

(31) Lin, R.-B.; Xiang, S.; Xing, H.; Zhou, W.; Chen, B. Exploration of porous metal−organic frameworks for gas separation and purification. *Coord. Chem. Rev.* **2019**, *378*, 87.

(32) Adil, K.; Belmabkhout, Y.; Pillai, R. S.; Cadiau, A.; Bhatt, P. M.; Assen, A. H.; Maurin, G.; Eddaoudi, M. Gas/vapour separation using ultra-microporous metal−organic frameworks: insights into the structure/separation relationship. *Chem. Soc. Rev.* **2017**, *46*, 3402.

(33) Jiao, L.; Seow, J. Y. R.; Skinner, W. S.; Wang, Z. U.; Jiang, H.-L. Metal−organic frameworks: Structures and functional applications. *Mater. Today* **2019**, *27*, 43.

(34) Zhao, X.; Wang, Y.; Li, D.-S.; Bu, X.; Feng, P. Metal−Organic Frameworks for Separation. *Adv. Mater.* **2018**, *30*, 1705189.

(35) Cui, Y.; Li, B.; He, H.; Zhou, W.; Chen, B.; Qian, G. Metal−Organic Frameworks as Platforms for Functional Materials. *Acc. Chem. Res.* **2016**, *49*, 483.

(36) Yang, X.; Xu, Q. Bimetallic Metal−Organic Frameworks for Gas Storage and Separation. *Cryst. Growth Des.* **2017**, *17*, 1450.

(37) Hendon, C. H.; Rieth, A. J.; Korzyński, M. D.; Dincă, M. Grand Challenges and Future Opportunities for Metal−Organic Frameworks. *ACS Cent. Sci.* **2017**, *3*, 554.

(38) Zheng, S.-T.; Bu, J. T.; Li, Y.; Wu, T.; Zuo, F.; Feng, P.; Bu, X. Pore Space Partition and Charge Separation in Cage-within-Cage Indium-Organic Frameworks with High CO_2 Uptake. *J. Am. Chem. Soc.* **2010**, *132*, 17062.

(39) Serre, C.; Mellot-Draznieks, C.; Surblé, S.; Audebrand, N.; Filinchuk, Y.; Férey, G. Role of Solvent-Host Interactions That Lead to Very Large Swelling of Hybrid Frameworks. *Science* **2007**, *315*, 1828.

(40) Horcajada, P.; Salles, F.; Wuttke, S.; Devic, T.; Heurtaux, D.; Maurin, G.; Vimont, A.; Daturi, M.; David, O.; Magnier, E.; Stock, N.; Filinchuk, Y.; Popov, D.; Riekel, C.; Férey, G.; Serre, C. How Linker's Modification Controls Swelling Properties of Highly Flexible Iron(III) Dicarboxylates MIL-88. *J. Am. Chem. Soc.* **2011**, *133*, 17839.

(41) Sudik, A. C.; Côté, A. P.; Yaghi, O. M. Metal-Organic Frameworks Based on Trigonal Prismatic Building Blocks and the New "acs" Topology. *Inorg. Chem.* **2005**, *44*, 2998.

(42) Zhao, X.; Bu, X.; Zhai, Q.-G.; Tran, H.; Feng, P. Pore Space Partition by Symmetry-Matching Regulated Ligand Insertion and Dramatic Tuning on Carbon Dioxide Uptake. *J. Am. Chem. Soc.* **2015**, *137*, 1396.

(43) Zhai, Q.-G.; Bu, X.; Zhao, X.; Li, D.-S.; Feng, P. Pore Space Partition in Metal−Organic Frameworks. *Acc. Chem. Res.* **2017**, *50*, 407.

(44) Assi, H.; Mouchaham, G.; Steunou, N.; Devic, T.; Serre, C. Titanium coordination compounds: from discrete metal complexes to metal−organic frameworks. *Chem. Soc. Rev.* **2017**, *46*, 3431.

(45) Zhu, J.; Li, P.-Z.; Guo, W.; Zhao, Y.; Zou, R. Titanium-based metal−organic frameworks for photocatalytic applications. *Coord. Chem. Rev.* **2018**, *359*, 80.

(46) Yuan, S.; Feng, L.; Wang, K.; Pang, J.; Bosch, M.; Lollar, C.; Sun, Y.; Qin, J.; Yang, X.; Zhang, P.; Wang, Q.; Zou, L.; Zhang, Y.; Zhang, L.; Fang, Y.; Li, J.; Zhou, H.-C. Stable Metal−Organic Frameworks: Design, Synthesis, and Applications. *Adv. Mater.* **2018**, *30*, 1704303.

(47) Wang, S.; Kitao, T.; Guillou, N.; Wahiduzzaman, M.; Martineau-Corcos, C.; Nouar, F.; Tissot, A.; Binet, L.; Ramsahye, N.; Devautour-Vinot, S.; Kitagawa, S.; Seki, S.; Tsutsui, Y.; Briois, V.;

Steunou, N.; Maurin, G.; Uemura, T.; Serre, C. A phase transformable ultrastable titanium-carboxylate framework for photoconduction. *Nat. Commun.* **2018**, *9*, 1660.

(48) Krishna, R. Screening metal−organic frameworks for mixture separations in fixed-bed adsorbers using a combined selectivity/capacity metric. *RSC Adv.* **2017**, *7*, 35724.

(49) Krishna, R. Methodologies for screening and selection of crystalline microporous materials in mixture separations. *Sep. Purif. Technol.* **2018**, *194*, 281.

(50) Pires, J.; Fernandes, J.; Dedecker, K.; Gomes, J. R. B.; Pérez-Sánchez, G.; Nouar, F.; Serre, C.; Pinto, M. L. Enhancement of Ethane Selectivity in Ethane−Ethylene Mixtures by Perfluoro Groups in Zr-Based Metal-Organic Frameworks. *ACS Appl. Mater. Interfaces* **2019**, *11*, 27410.

(51) Wang, X.; Niu, Z.; Al-Enizi, A. M.; Nafady, A.; Wu, Y.; Aguila, B.; Verma, G.; Wojtas, L.; Chen, Y.-S.; Li, Z.; Ma, S. Pore environment engineering in metal−organic frameworks for efficient ethane/ethylene separation. *J. Mater. Chem. A* **2019**, *7*, 13585.

https://dx.doi.org/10.1021/jacs.9b12924
J. Am. Chem. Soc. 2020, 142, 2222−2227

Pore-Space-Partition-Enabled Exceptional Ethane Uptake and Ethane-Selective Ethane-Ethylene Separation

Huajun Yang,[a,b] Yanxiang Wang,[b] Rajamani Krishna,*[c] Xiaoxia Jia,[b] Yong Wang,[b] Anh N. Hong,[b] Candy Dang,[a] Henry E. Castillo,[a] and Xianhui Bu,*[a] Pingyun Feng*[b]

[a] Department of Chemistry and Biochemistry, California State University, Long Beach, California 90840, United States

[b] Department of Chemistry, University of California, Riverside, California 92521, United States

[c] Van't Hoff Institute for Molecular Sciences, University of Amsterdam, Science Park 904, 1098 XH Amsterdam, The Netherland

EXPERIMENTAL SECTION

Synthesis of [$Co_2TiO(bdc)_3tpt$] (Co_2Ti-bdc-tpt or CPM-723, CCDC No. 1967757). In a 15 mL glass vial, 52 mg of cobalt chloride ($CoCl_2$, ~0.4 mmol), 50 mg titanocene dichloride (Cp_2TiCl_2, ~0.2 mmol) 100 mg 1,4-benzenedicarboxylic acid (H_2BDC, ~0.4 mmol), and 62 mg 2,4,6-tri(4-pyridyl)-1,3,5-triazine (tpt, ~0.2 mmol) were dissolved in 3.0 g dimethylformamide (DMF). After being stirred for an hour, the vial was placed in a 130 ℃ oven for 3 days, and the mixture was then cooled to room temperature. Large red polyhedral crystals with small amount of colorless recrystallized organic ligands were obtained. The organic ligands can be removed by being refluxed in dichloromethane for around 12 hours. The phase purity was supported by powder X-ray diffraction.

Synthesis of [$Co_2V(OH)(bdc)_3tpt$] (Co_2V-bdc-tpt or CPM-733, CCDC No. 1967755). In a 15 mL glass vial, 120 mg of cobalt nitrate hexahydrate ($Co(NO_3)_2\cdot 6H_2O$, ~0.4 mmol), 32 mg vanadium (III) chloride (VCl_3, ~0.2 mmol), 100 mg 1,4-benzenedicarboxylic acid (H_2BDC, ~0.6 mmol), and 62 mg 2,4,6-tri(4-pyridyl)-1,3,5-triazine (tpt, ~0.2 mmol) were dissolved in 3.0 g dimethylformamide (DMF). After being stirred for an hour, the vial was placed in a 130 ℃ oven for 3 days, and the mixture was then cooled to room temperature. Dark-red spindle-shaped crystals were obtained. The phase purity was supported by powder X-ray diffraction.

Synthesis of [$Co_2V(OH)(1,4\text{-ndc})_3tpt$] ($Co_2V$-ndc-tpt or CPM-736). In a 15 mL glass vial, 52 mg of cobalt chloride ($CoCl_2$, ~0.4 mmol), 32 mg vanadium (III) chloride (VCl_3, ~0.2 mmol), 130 mg 1,4-naphthalenedicarboxylic acid (1,4-H_2NDC, ~0.6 mmol), and 62 mg 2,4,6-tri(4-pyridyl)-1,3,5-triazine (tpt, ~0.2 mmol) were dissolved in 3.0 g dimethylformamide (DMF). After being stirred for an hour, the vial was placed in a 130 °C oven for 3 days, and the mixture was then cooled to room temperature. Microcrystalline dark-red spindle-shaped crystals were obtained. The phase purity was supported by powder X-ray diffraction.

Synthesis of [$Co_2V(OH)(dmbdc)_3tpt$] (Co_2V-dmbdc-tpt or CPM-738). In a 15 mL glass vial, cobalt nitrate hexahydrate ($Co(NO_3)_2{\cdot}6H_2O$, ~0.4 mmol), 32 mg vanadium (III) chloride (VCl_3, ~0.2 mmol), 117 mg 2,5-dimethylterephthalic acid (H_2DMBDC, ~0.6 mmol), and 62 mg 2,4,6-tri(4-pyridyl)-1,3,5-triazine (tpt, ~0.2 mmol) were dissolved in 3.0 g dimethylformamide (DMF). After being stirred for an hour, the vial was placed in a 130 °C oven for 3 days, and the mixture was then cooled to room temperature. Microcrystalline dark-red spindle-shaped crystals were obtained. The phase purity was supported by powder X-ray diffraction.

Synthesis of [$Mg_2TiO(bdc)_3tpbz$] (Mg_2Ti-bdc-tpbz or CPM-223-tpbz, CCDC No. 1967758). In a 15 mL glass vial, 30 mg of magnesium chloride hexahydrate ($MgCl_2{\cdot}6H_2O$, ~0.15 mmol), 37 mg titanocene dichloride (Cp_2TiCl_2, ~0.15 mmol), 50 mg 1,4-benzenedicarboxylic acid (H_2BDC, ~0.3 mmol), and 31 mg 2,4,6-tri(4-pyridyl)benzene (tpbz, 0.1 mmol) were dissolved in 3.0 g dimethylformamide (DMF). After being stirred for an hour, the vial was placed in a

120 °C oven for 4 days, and the mixture was then cooled to room temperature. Large grey truncated hexagonal prism crystals were obtained. The phase purity was supported by powder X-ray diffraction.

Synthesis of [$Mg_2TiO(bdc)_3tppy$] (Mg_2Ti-bdc-tppy or CPM-223-tppy, CCDC No. 1967759). In a 15 mL glass vial, 30 mg of magnesium chloride hexahydrate ($MgCl_2·6H_2O$, ~0.15 mmol), 37 mg titanocene dichloride (Cp_2TiCl_2, ~0.15 mmol), 50 mg 1,4-benzenedicarboxylic acid (H_2BDC, ~0.3 mmol), and 31 mg 2,4,6-tri(4-pyridyl)pyridine (tpp, 0.1 mmol) were dissolved in 3.0 g dimethylformamide (DMF). After being stirred for an hour, the vial was placed in a 120 °C oven for 4 days, and the mixture was then cooled to room temperature. Large grey truncated hexagonal prism crystals were obtained. The phase purity was supported by powder X-ray diffraction.

Synthesis of [$Mg_2TiO(bdc)_3tpt$] (Mg_2Ti-bdc-tpt or CPM-223, CCDC No. 1967756). The microcrystalline sample of CPM-223 was originally reported in Ref. [S1]. Here, with the following modified procedure, we could get large-sized crystals which are suitable for single crystal X-ray diffraction. In a 15 mL glass vial, 30 mg of magnesium chloride hexahydrate ($MgCl_2·6H_2O$, ~0.15 mmol), 37 mg titanocene dichloride (Cp_2TiCl_2, ~0.15 mmol), 75 mg 1,4-benzenedicarboxylic acid (H_2BDC, ~0.3 mmol), and 31 mg 2,4,6-tri(4-pyridyl)-1,3,5-triazine (tpt, ~0.1 mmol) were dissolved in 3.0 g dimethylformamide (DMF). After being stirred for an hour, the vial was placed in a 120 °C oven for 4 days, and the mixture was then cooled to room temperature. Large grey truncated hexagonal prism crystals were obtained. The phase purity was supported by powder X-ray diffraction.

Synthesis of [$Mg_2V(OH)(bdc)_3tpt$] (Mg_2V-bdc-tpt or CPM-233, CCDC No. 1967761). The microcrystalline sample of CPM-233 was originally reported in ref. [S1]. Here, with the following modified procedure, we could get large-sized crystals which are suitable for single crystal X-ray diffraction. In a 15 mL glass vial, 40 mg of magnesium chloride hexahydrate ($MgCl_2{\cdot}6H_2O$, ~0.2 mmol), 16 mg vanadium chloride (VCl_3, ~0.1 mmol), 50 mg 1,4-benzenedicarboxylic acid (H_2BDC, ~0.3 mmol), and 31 mg 2,4,6-tri(4-pyridyl)-1,3,5-triazine (tpt, ~0.1 mmol) were dissolved in 3.0 g dimethylformamide (DMF). 1 drop of concentrated hydrochloric acid (around 25 μL) was subsequently added. After being stirred for an hour, the vial was placed in a 120 ℃ oven for 4 days, and the mixture was then cooled to room temperature. Pink block crystals were obtained. The phase purity was supported by powder X-ray diffraction.

Synthesis of [$Mg_2V(OH)(dmbdc)_3tpt$] (Mg_2V-dmbdc-tpt or CPM-238, CCDC No. 1967760). In a 15 mL glass vial, 40 mg of magnesium chloride hexahydrate ($MgCl_2{\cdot}6H_2O$, ~0.2 mmol), 16 mg vanadium chloride (VCl_3, ~0.1 mmol), 58 mg 2,5-dimethylterephthalic acid (H_2DMBDC, ~0.3 mmol), and 31 mg 2,4,6-tri(4-pyridyl)-1,3,5-triazine (tpt, ~0.1 mmol) were dissolved in 3.0 g dimethylformamide (DMF). 1 drop of concentrated hydrochloric acid (around 25 μL) was subsequently added. After being stirred for an hour, the vial was placed in a 120

°C oven for 4 days, and the mixture was then cooled to room temperature. Pink block crystals were obtained. The phase purity was supported by powder X-ray diffraction.

Single-Crystal X-ray Diffraction Characterization. The single-crystal X-ray diffraction measurements were performed on a Bruker diffractometer using graphite-monochromated MoKα (λ= 0.71073 Å) radiation at room temperature. Diffraction data were integrated and scaled by 'multi-scan' method with the Bruker APEX software. The structure was solved by intrinsic phasing which was embedded in 'APEX III' software and the refinement against all reflections of the compound was performed using 'APEX III'. All non-hydrogen framework atoms were refined anisotropically. All the hydrogen atoms were calculated. CCDC 1967756-1967761 contain the supplementary crystallographic data for this paper. These data are provided free of charge by the Cambridge Crystallographic Data Centre.

Powder X-ray Diffraction (PXRD) Characterization. Powder X-ray diffraction experiments were performed on a PANalytical X'Pert Pro MPD diffractometer, equipped with a linear X'Celerator detector, which was operating at 40 kV and 35 mA (Cu Kα radiation, λ = 1.5418 Å). The data collection was performed at room temperature in the range from 5° to 40° with a step size of ~0.008°. The simulated powder pattern was obtained from the single crystal data.

Thermogravimetric (TG) Measurement. A TA Instruments TGA Q500 thermal analyzer was used to measure the TG curve by heating the sample from 30 °C to 800 °C with heating rate of 5°C/min under nitrogen flow. The flow rate of the nitrogen gas was controlled at about 60 milliliters per minute.

Water Stability Tests for CPM-723 (Co_2Ti-bdc-tpt) and CPM-733 (Co_2Ti-bdc-tpt). In one batch, around 10 mg of samples were immersed in 10 mL of water at room temperature. After 24 hours, the samples were washed by methanol and dried in 80 °C oven for PXRD experiments.

Thermal Stability Tests for CPM-223. Around 10 mg of samples were heated from room temperature to different temperatures with a heating rate of 10°C/min under nitrogen flow using TGA Q500 instrument. The samples were kept at targeted temperature for one hour and then were allowed to be cooled to room temperature naturally. The processed samples were then subject to PXRD experiments.

Energy dispersive spectroscopy (EDS). The semi-quantitative elemental analyses of different heterometallic MOF samples were performed by using a FEI NNS450 field emission scanning electron microscope equipped with 50 mm^2 X-Max50 SDD energy dispersive spectroscopy (EDS) detector. Data acquisition was performed with an accelerating voltage of 15 kV and 20 s accumulation time.

X-ray Photoelectron Spectroscopy (XPS). XPS characterization was carried out by using a Kratos AXIS ULTRADLD XPS system equipped with an Al Kα monochromated X-ray source and a 165-mm mean radius electron energy hemispherical analyzer.

Gas Sorption Measurement. Gas sorption measurements were carried out on a Micromeritics ASAP 2020 and ASAP 2020 PLUS Physisorption Analyzers. Prior to the measurement, the as-synthesized sample was purified by DMF and immersed in dichloromethane (extra dry) for three days. During each day, the solution was refreshed. After solvent exchange, the upper solvent was decanted. The sample was first dried under air flow gently and was subsequently transferred into the test tube. The degas process was performed under room temperature for 2 hours and further dried at 80 ºC for another 10 hours. Notably, longer exposure time to air will reduce the gas uptake, especially for magnesium crystals. The BET surface area of all the samples was calculated from the N_2 adsorption isotherm with the pressure range of $P/P_0 < 0.1$ due to the microporous pore.

Isosteric Heat of Adsorption (Q_{st}). The isosteric heats of adsorption for all the gases were calculated using the isotherms at 273 K and 298 K, following the Clausius-Clapeyron equation. It was done with the calculation program embedded in the software of ASAP 2020 plus. High accuracy of the Q_{st} was found in all the calculations as evidenced by the linearity in the isosters.

Selectivity by IAST. To evaluate the C_2H_6/C_2H_4 separation performance, the selectivity was calculated by ideal adsorbed solution theory (IAST). Single-site Langmuir-Freundlich (SLF) model was employed to fit the gas adsorption isotherms over the entire pressure range. SLF model can be written as:

$$N = \frac{N_{sat} b p^{1/n}}{1 + b p^{1/n}} \tag{1}$$

Where N is the quantity adsorbed, p is the pressure of bulk gas at equilibrium with adsorbed phase, N_{sat} is the saturation loadings for adsorption site, and b are the affinity parameters. 1/n is the index of heterogeneity. The R factors for all the fitting are higher than 99.9%.

The detailed methodology for calculating the amount of A and B adsorption from a mixture by IAST is described elsewhere.[S2] The adsorption selectivity is finally defined as:

$$selectivity = \frac{q_A / q_B}{p_A / p_B} \tag{2}$$

where q_i (i = A or B) is the uptake quantity in the mixture and p_i is the feeding partial pressure of component i.

Separation Potential.[S3] The separation potential (ΔQ) is a combined metric, which considering both uptake capacity and selectivity. It is defined to quantify mixture separations in fixed bed adsorbers. For a C_2H_6/C_2H_4 mixture with mole fractions y_{C2H6}, and y_{C2H4}=1-y_{C2H6}, the gravimetric separation potential ΔQ, is calculated from IAST using the formula

$$\Delta Q = q_{C2H6}\frac{y_{C2H4}}{1-y_{C2H4}} - q_{C2H4} \tag{3}$$

where q_{C2H6} and q_{C2H4} are C_2H_6 and C_2H_4 uptake in the mixture, respectively, which are calculated based on IAST theory. For 50/50 mixture, the formula (3) can be simplified as

$$\Delta Q = q_{C2H6} - q_{C2H4} \tag{4}$$

The physical significance of ΔQ is that it represents the maximum amount of pure C_2H_4 that can be recovered during the adsorption phase of fixed bed separations.

GCMC Simulation. The GCMC calculations were performed by SORPTION code embedded in the Material Studio (MS) software. Periodic boundary conditions were applied in three dimensions. In addition, the force field of the condensed phase optimized molecular potential for atomistic simulation studies (COMPASS), was used to describe the interatomic interaction. Specifically, the van der Waals interactions with a cutoff of 12 Å were depicted by the Lennard−Jones potential and the electrostatic interactions were described via the Ewald summation method.

DFT calculation. The initial positions of the gas molecules were first estimated by GCMC simulation. The cluster model was cleaved from the unit cell of Co_2V-bdc-tpt. The dangling bonds were saturated by H. The DFT (DFT-D2) calculations were performed to describe the interaction between the clusters and gas molecules (ethylene or ethane) using DMol^3 module that was implemented in Materials Studio.[S4,5] **The Perdew–Burke–Ernzerhof (PBE) exchange-correlation potential combined with the double numerical basis set containing polarization function (DNP) was employed in the calculations. Core electrons were used to set the type of core treatment. The convergence threshold parameters for the optimization were 10^{-5} Ha (energy), 2×10^{-3} Ha/Å (gradient), and 5×10^{-3} Å (displacement), respectively.**

The binding energy (BE) between the gas molecules and MOFs was calculated as follows:

$$\Delta E = E_{\mathrm{MOFs-gas}} - E_{\mathrm{MOFs}} - E_{\mathrm{gas}} \quad (5)$$

where E represents the energy of the system after geometry relaxation, $E_{\mathrm{MOFs-gas}}$ is the total energy of the MOFs and gas molecules, E_{MOFs} and E_{gas} are the energies of the isolated MOFs and gas molecules, respectively.

Transient Breakthrough Simulation. To determine the productivity of polymer-grade (99.95%) C_2H_4, we performed transient breakthrough simulations using the simulation methodology described in our previous publications.[S3,6] For the breakthrough simulations, the following parameter values were used: length of packed bed, L = 0.3 m; voidage of packed bed, ε = 0.4; superficial gas velocity at inlet, u = 0.04 m/s. The transient breakthrough simulation results are presented in terms of a dimensionless time, τ, defined by dividing the actual time, t, by the characteristic time, $L\varepsilon u^{-1}$.

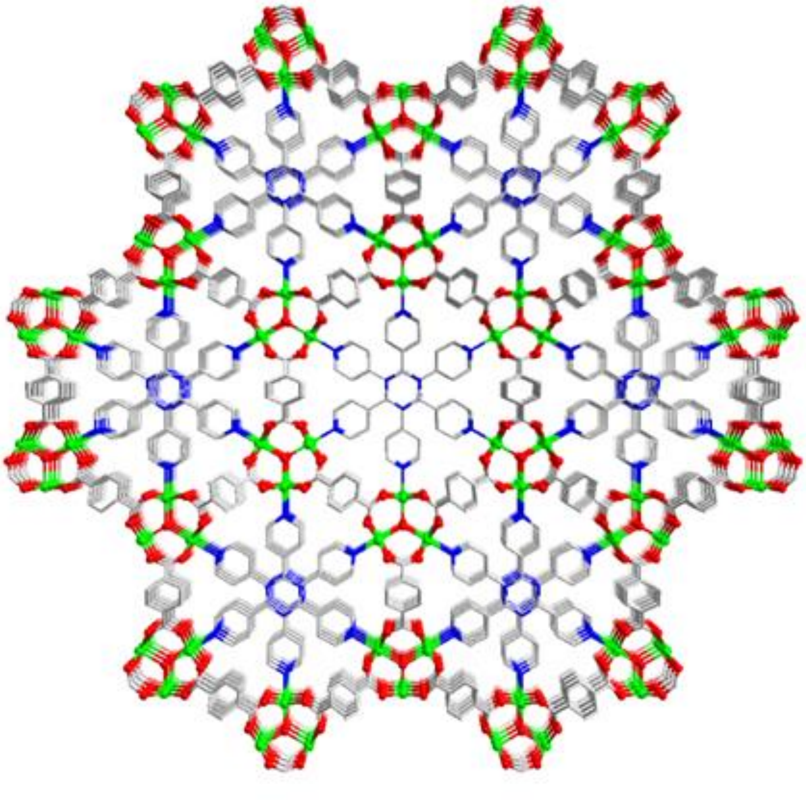

Figure S1. Illustration of *pacs*-tpt structure. Metal, green; oxygen, red; carbon, grey; nitrogen, blue.

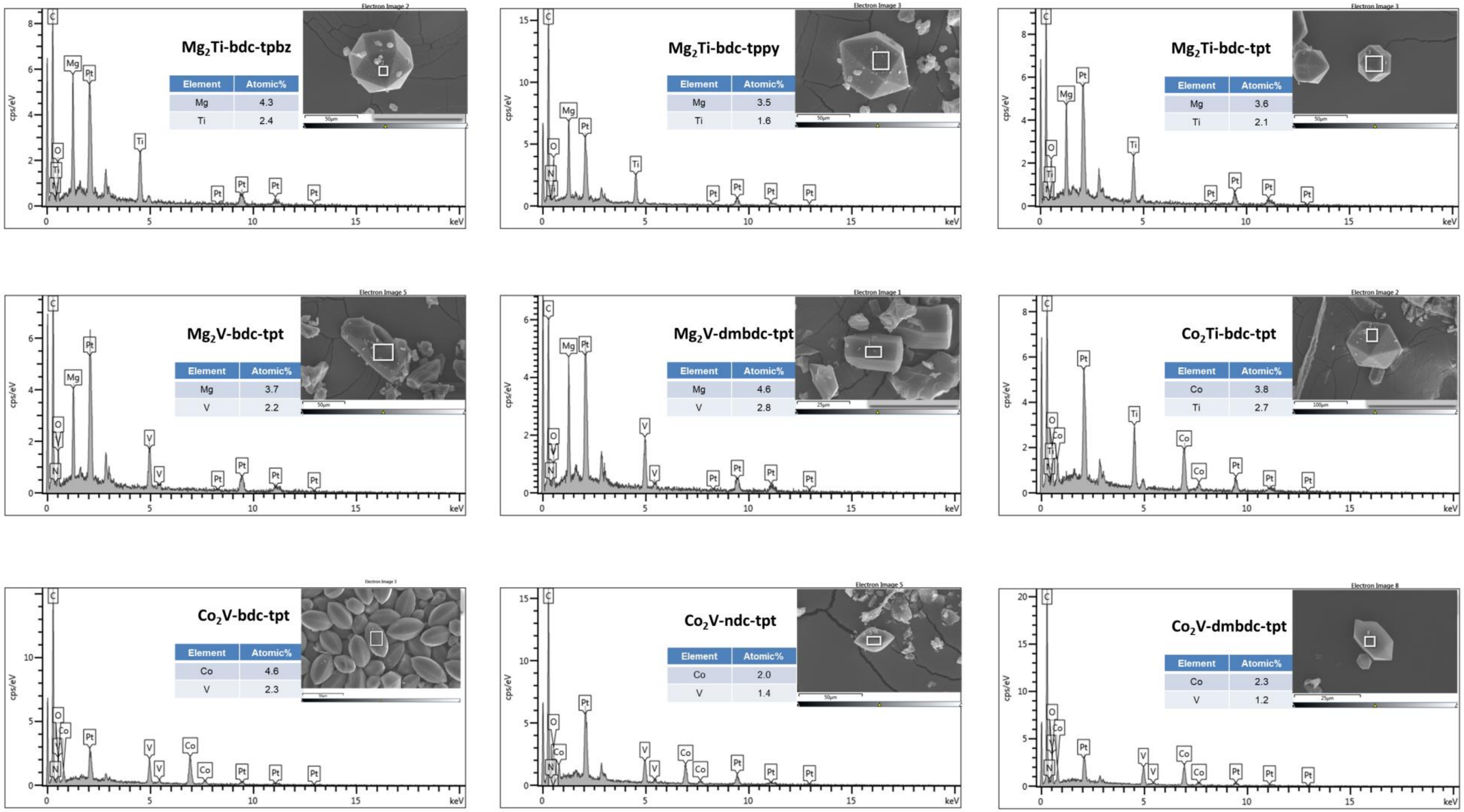

Mg_2Ti-bdc-tpbz

Element	Atomic%
Mg	4.3
Ti	2.4

Mg_2Ti-bdc-tppy

Element	Atomic%
Mg	3.5
Ti	1.6

Mg_2Ti-bdc-tpt

Element	Atomic%
Mg	3.6
Ti	2.1

Mg_2V-bdc-tpt

Element	Atomic%
Mg	3.7
V	2.2

Mg_2V-dmbdc-tpt

Element	Atomic%
Mg	4.6
V	2.8

Co_2Ti-bdc-tpt

Element	Atomic%
Co	3.8
Ti	2.7

Co_2V-bdc-tpt

Element	Atomic%
Co	4.6
V	2.3

Co_2V-ndc-tpt

Element	Atomic%
Co	2.0
V	1.4

Co_2V-dmbdc-tpt

Element	Atomic%
Co	2.3
V	1.2

Figure S2. EDS analysis of all the MOFs in this study. The atomic ratios of the metals are shown.

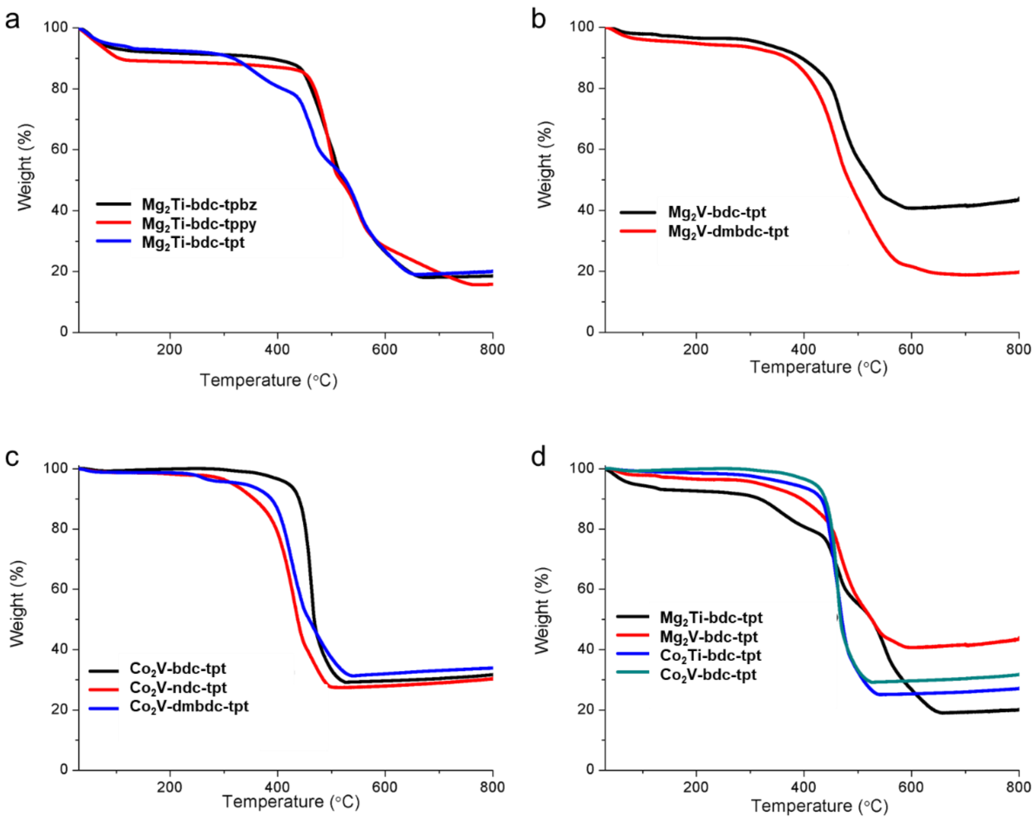

Figure S3. Comparisons of TGA traces of activated samples for all the compounds in this study. a: TGA traces of Mg_2Ti-bdc MOFs with different ligand 2 ; b: TGA traces of Mg_2V-bdc MOFs with different ligand 1; c: TGA traces of Co2V-tpt MOFs with different ligand 1; d: TGA traces of bdc-tpt MOFs with different metal trimers.

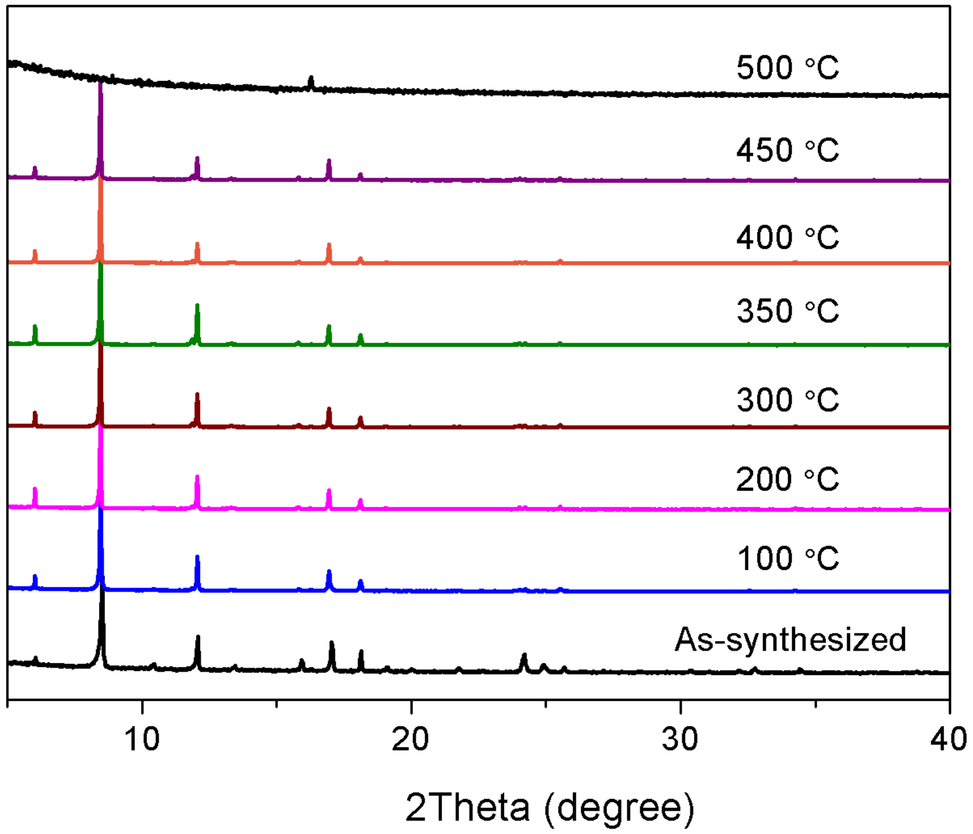

Figure S4. PXRD patterns of CPM-223 under different thermal treatments.

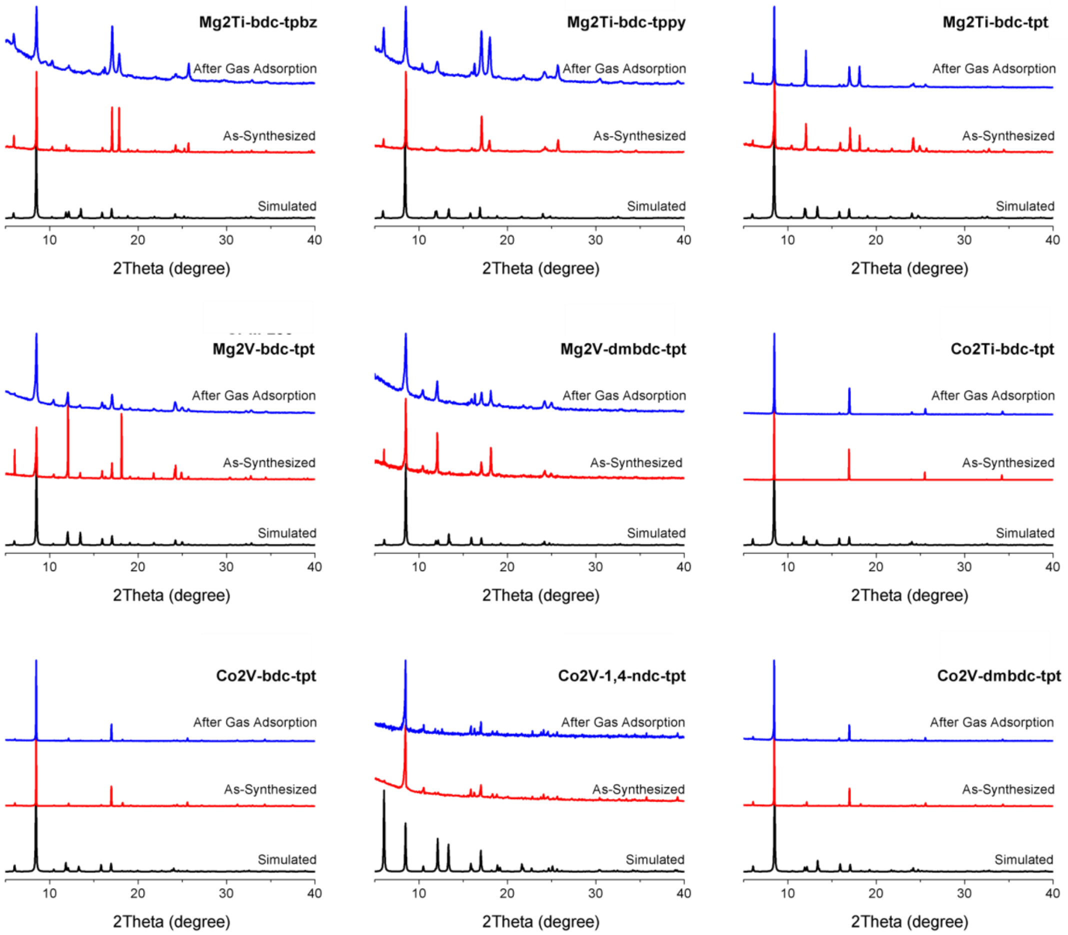

Figure S5. Experimental and simulated PXRD patterns for all the compounds in this study. For Co_2V-ndc-tpt and Co_2V-dmbdc-tpt, the simulated PXRD were generated from Mg_2V-ndc-tpt and Mg_2V-dmbdc-tpt, respectively, for comparison.

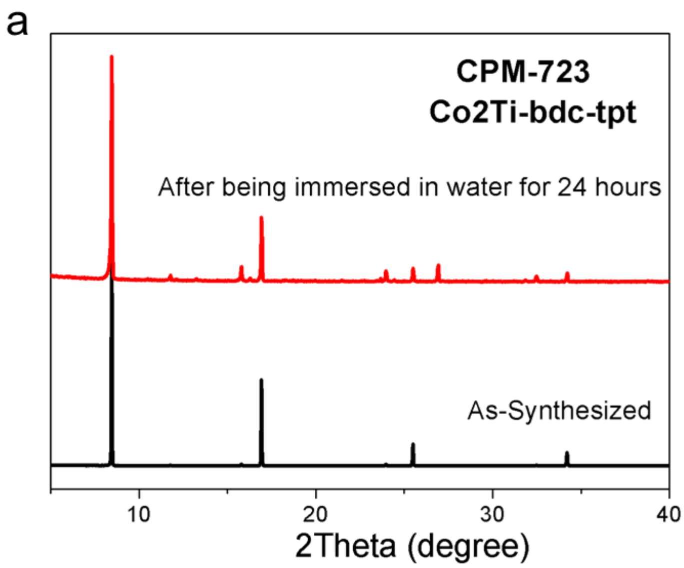

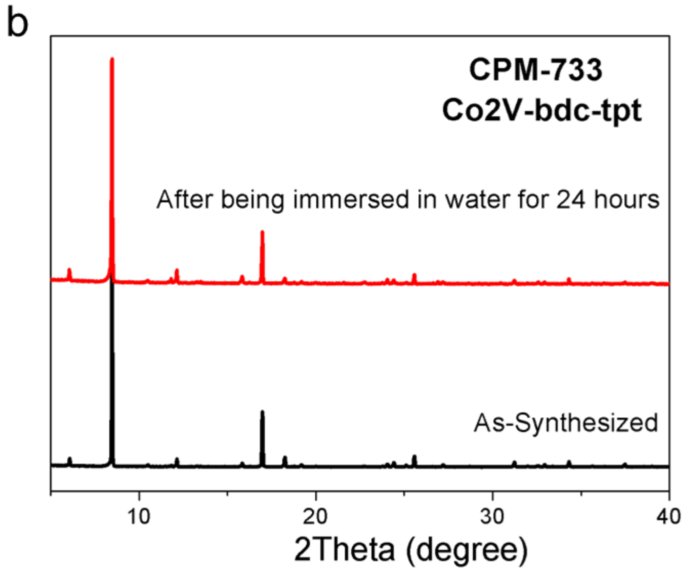

Figure S6. Comparisons of PXRD patterns of as-synthesized samples and the samples after being immersed in water for 24 hours (a: CPM-723; b: CPM-733).

For this family of structures, the occupation of open metal sites by pore-partitioning ligands prevents the water attack on the open metal site, suppresses the breathing effect of MIL-88-type structure, and increases the framework connectivity simultaneously. Such rigidification leads to the robust nature.

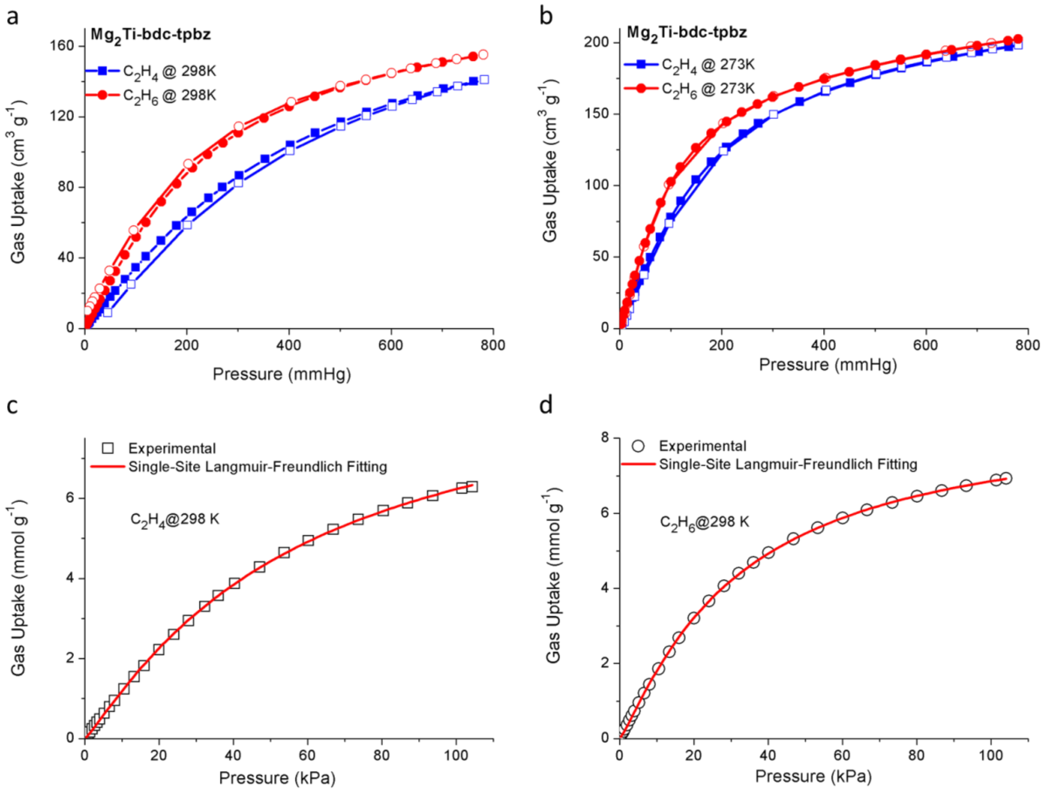

Figure S7. Gas adsorption properties for Mg_2Ti-bdc-tpbz. a: C_2H_4 adsorption and C_2H_6 adsorption at 298 K; b: C_2H_4 adsorption and C_2H_6 adsorption at 273 K; c: SLF fitting for C_2H_4 adsorption at 298 K; d: SLF fitting for C_2H_6 adsorption at 298 K.

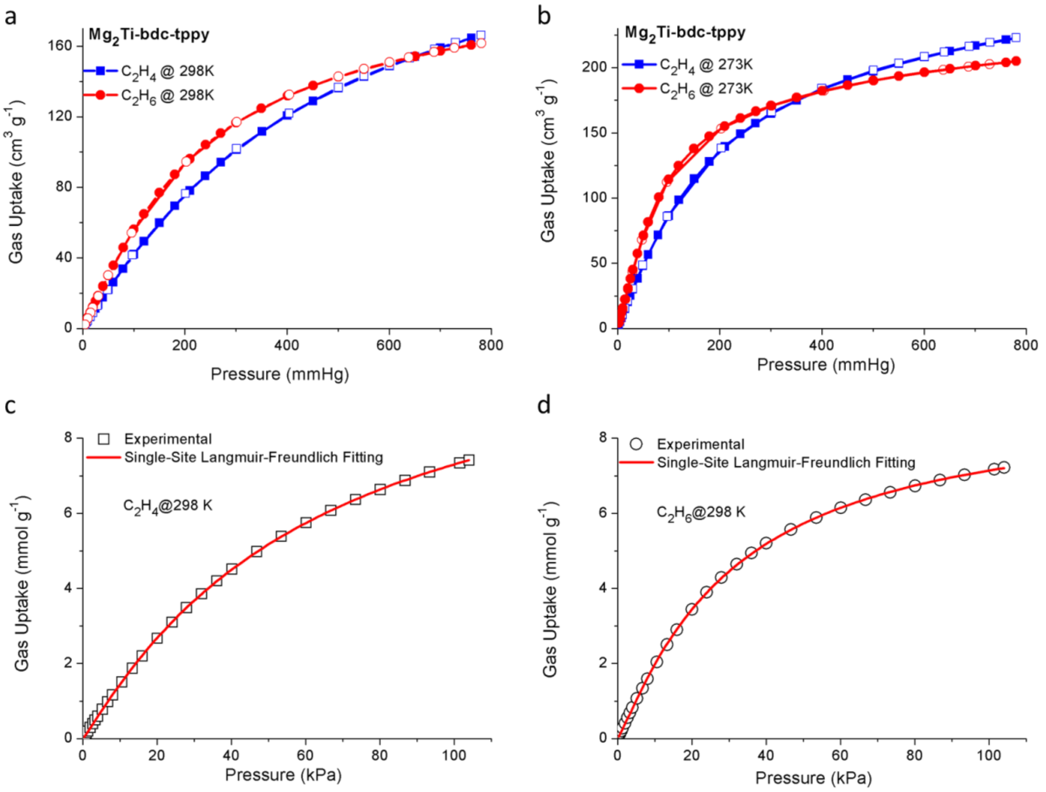

Figure S8. Gas adsorption properties for Mg2Ti-bdc-tppy. a: C_2H_4 adsorption and C_2H_6 adsorption at 298 K; b: C_2H_4 adsorption and C_2H_6 adsorption at 273 K; c: SLF fitting for C_2H_4 adsorption at 298 K; d: SLF fitting for C_2H_6 adsorption at 298 K.

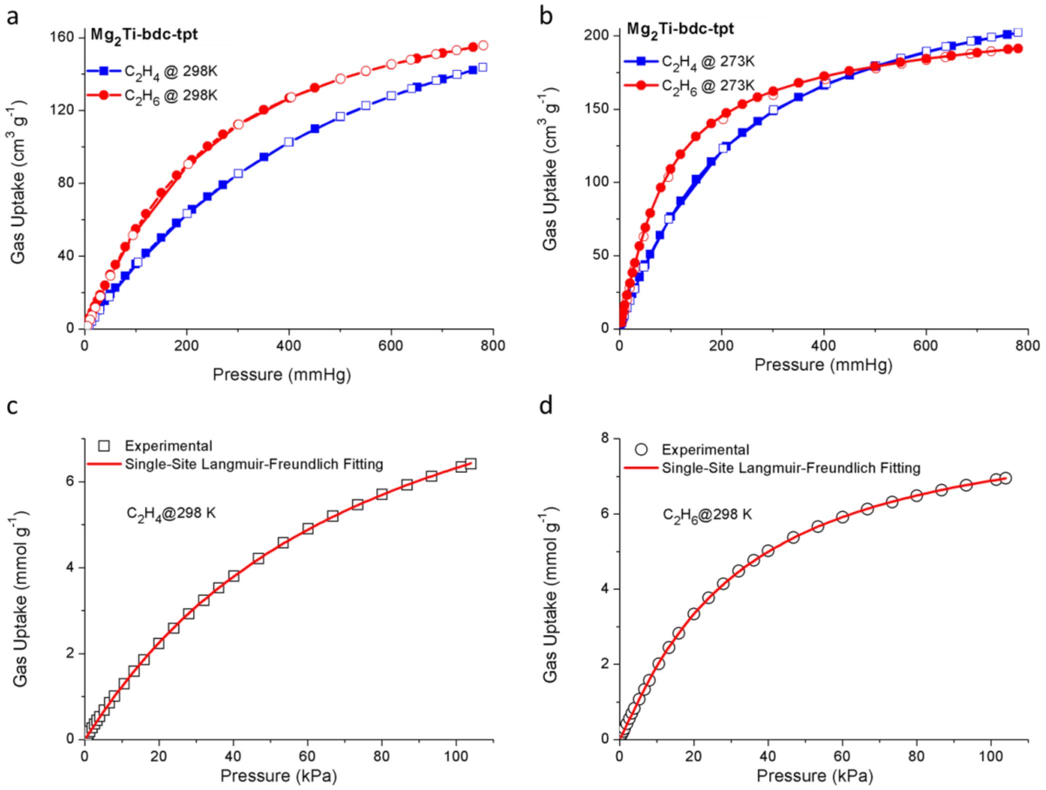

Figure S9. Gas adsorption properties for Mg$_2$Ti-bdc-tpt. a: C_2H_4 adsorption and C_2H_6 adsorption at 298 K; b: C_2H_4 adsorption and C_2H_6 adsorption at 273 K; c: SLF fitting for C_2H_4 adsorption at 298 K; d: SLF fitting for C_2H_6 adsorption at 298 K.

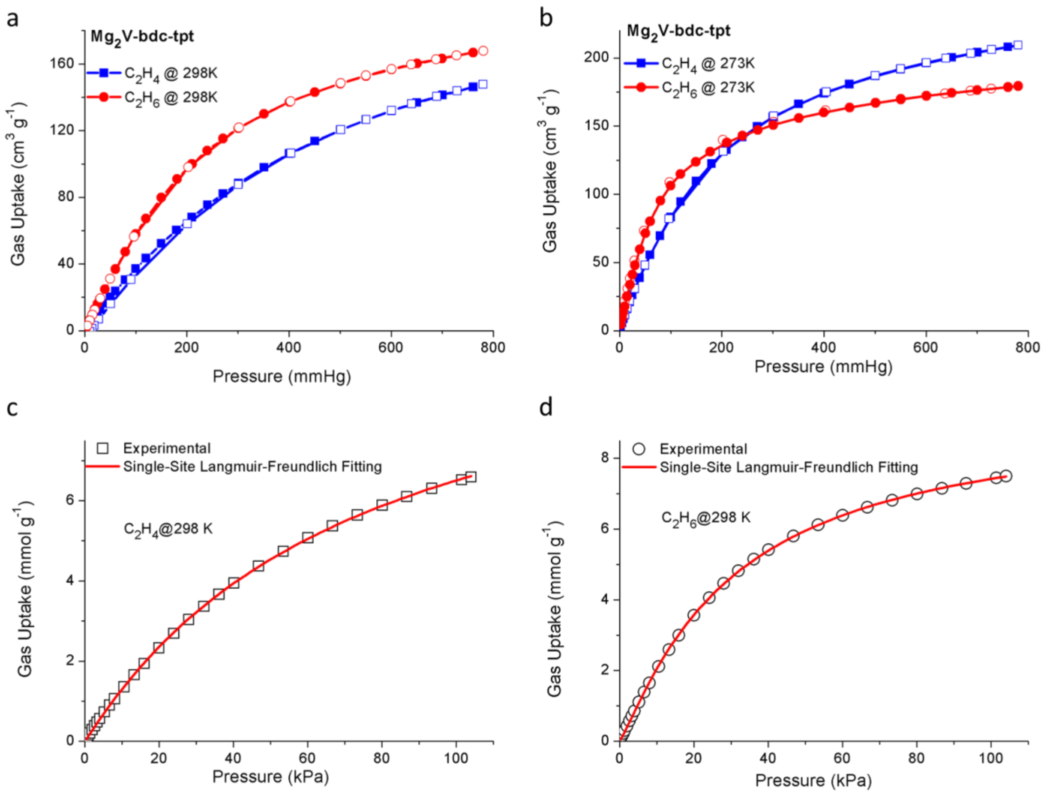

Figure S10. Gas adsorption properties for Mg2V-bdc-tpt. a: C_2H_4 adsorption and C_2H_6 adsorption at 298 K; b: C_2H_4 adsorption and C_2H_6 adsorption at 273 K; c: SLF fitting for C_2H_4 adsorption at 298 K; d: SLF fitting for C_2H_6 adsorption at 298 K.

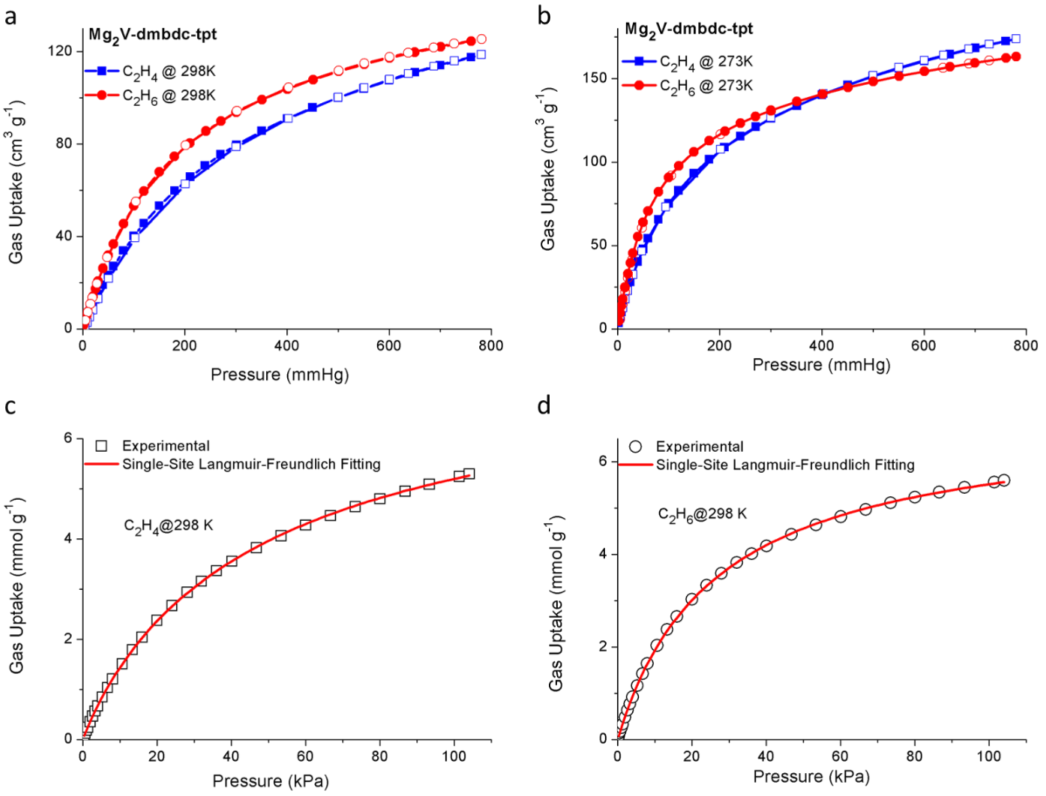

Figure S11. Gas adsorption properties for Mg_2V-bdc-tpt. a: C_2H_4 adsorption and C_2H_6 adsorption at 298 K; b: C_2H_4 adsorption and C_2H_6 adsorption at 273 K; c: SLF fitting for C_2H_4 adsorption at 298 K; d: SLF fitting for C_2H_6 adsorption at 298 K.

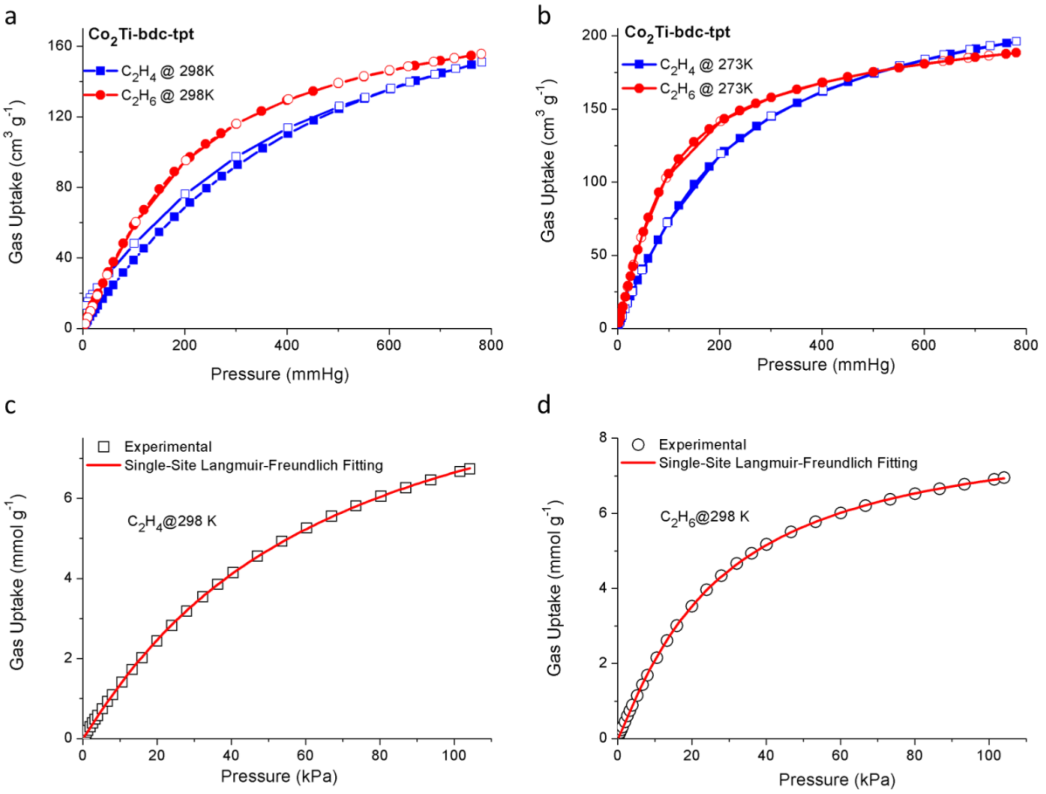

Figure S12. Gas adsorption properties for Co_2Ti-bdc-tpt. a: C_2H_4 adsorption and C_2H_6 adsorption at 298 K; b: C_2H_4 adsorption and C_2H_6 adsorption at 273 K; c: heat of adsorption for C_2H_4 and C_2H_6; d: N_2 adsorption at 77 K; e: SLF fitting for C_2H_4 adsorption at 298 K; f: SLF fitting for C_2H_6 adsorption at 298 K.

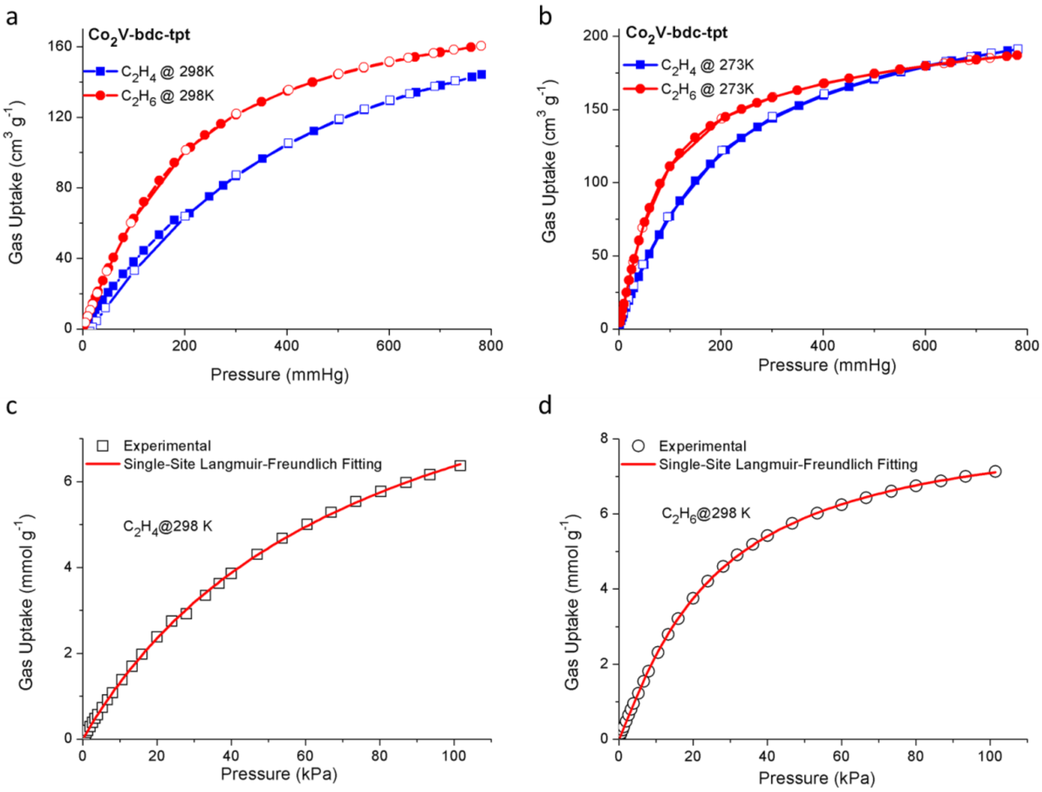

Figure S13. Gas adsorption properties for Co$_2$V-bdc-tpt. a: C_2H_4 adsorption and C_2H_6 adsorption at 298 K; b: C_2H_4 adsorption and C_2H_6 adsorption at 273 K; c: SLF fitting for C_2H_4 adsorption at 298 K; d: SLF fitting for C_2H_6 adsorption at 298 K.

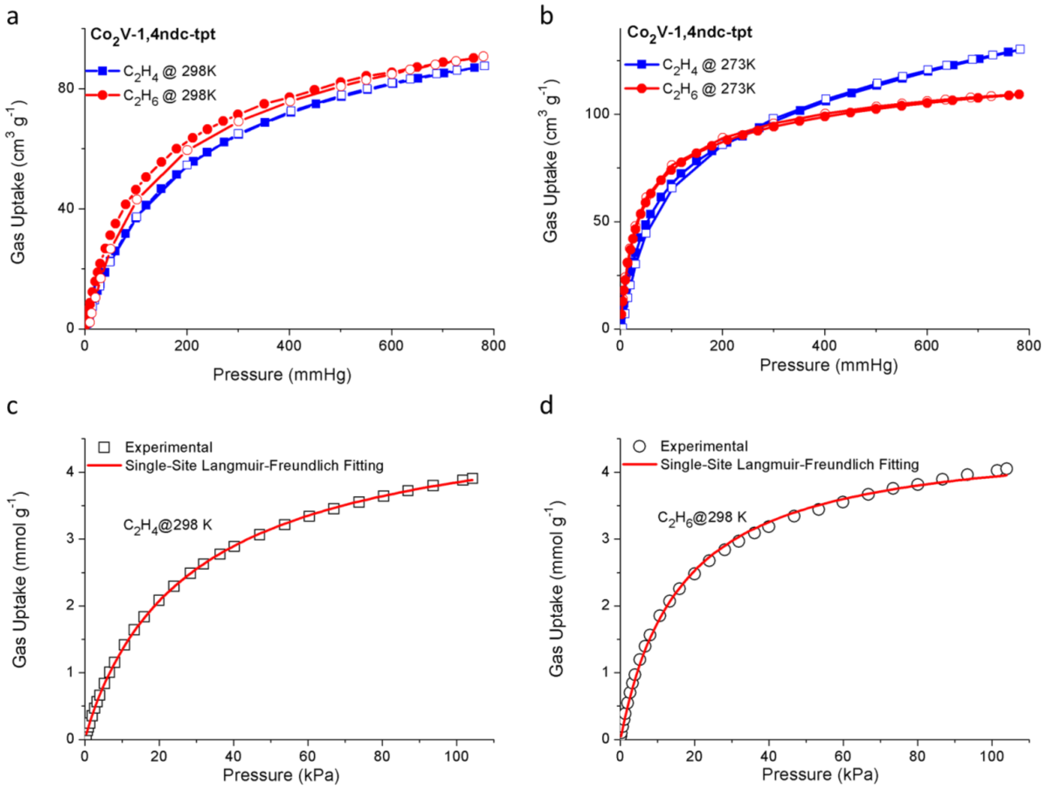

Figure S14. Gas adsorption properties for Co_2V-ndc-tpt. a: C_2H_4 adsorption and C_2H_6 adsorption at 298 K; b: C_2H_4 adsorption and C_2H_6 adsorption at 273 K; c: heat of adsorption for C_2H_4 and C_2H_6; d: N_2 adsorption at 77 K; e: SLF fitting for C_2H_4 adsorption at 298 K; f: SLF fitting for C_2H_6 adsorption at 298 K.

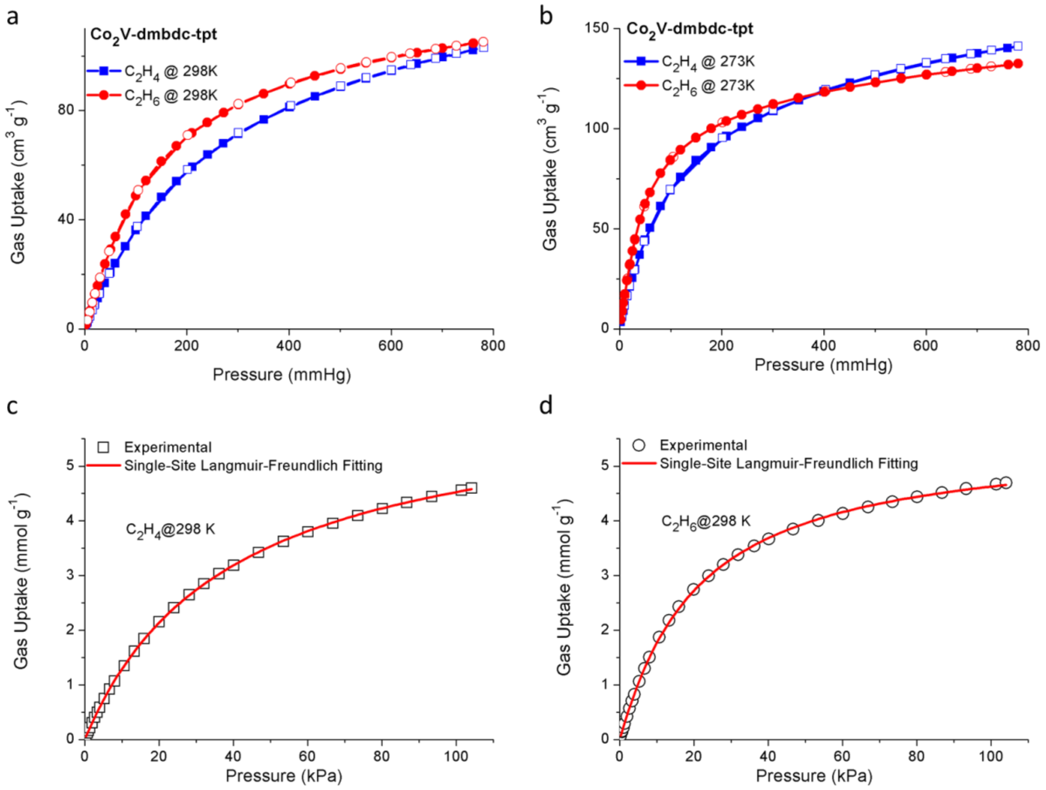

Figure S15. Gas adsorption properties for Co$_2$V-dmbdc-tpt. a: C_2H_4 adsorption and C_2H_6 adsorption at 298 K; b: C_2H_4 adsorption and C_2H_6 adsorption at 273 K; c: heat of adsorption for C_2H_4 and C_2H_6; d: N_2 adsorption at 77 K; e: SLF fitting for C_2H_4 adsorption at 298 K; f: SLF fitting for C_2H_6 adsorption at 298 K.

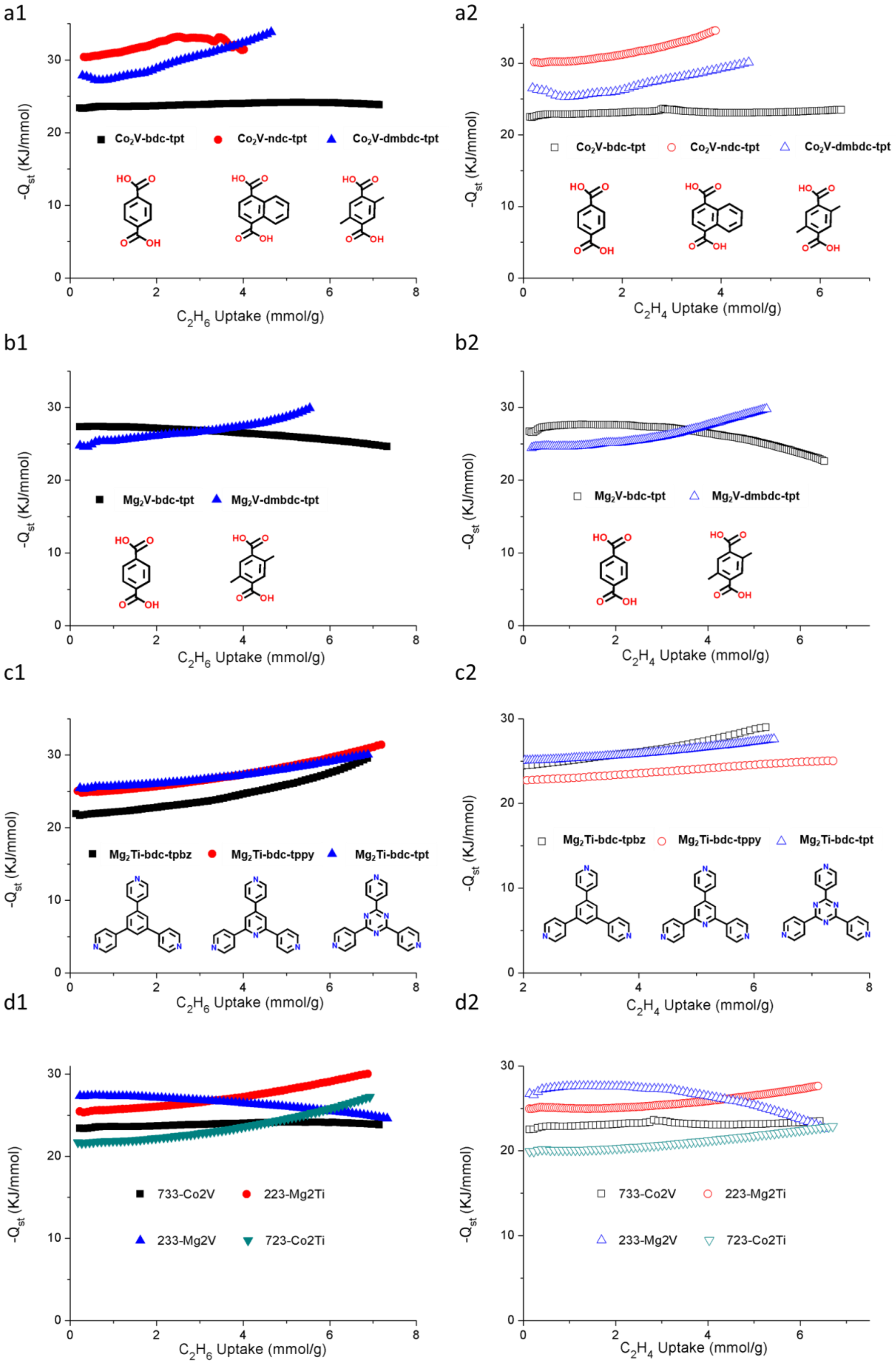

Figure S16. Comparisons of adsorption enthalpy for C_2H_6 and C_2H_4 adsorption.

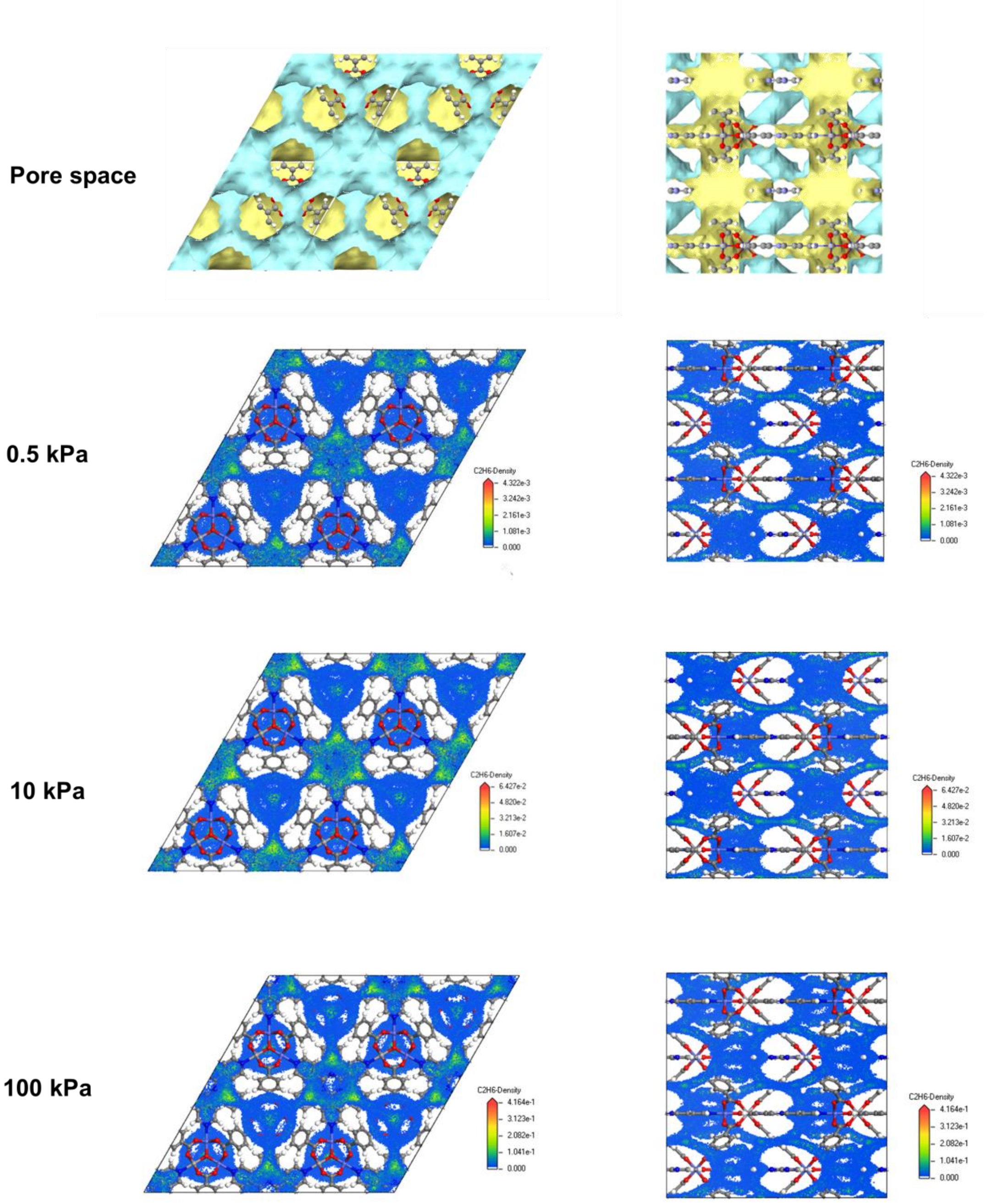

Figure S17. Density distribution of C_2H_6 molecules mass center within Co_2V-bdc-tpt under different pressures from GCMC simulations. Pore surface is also shown for comparison.

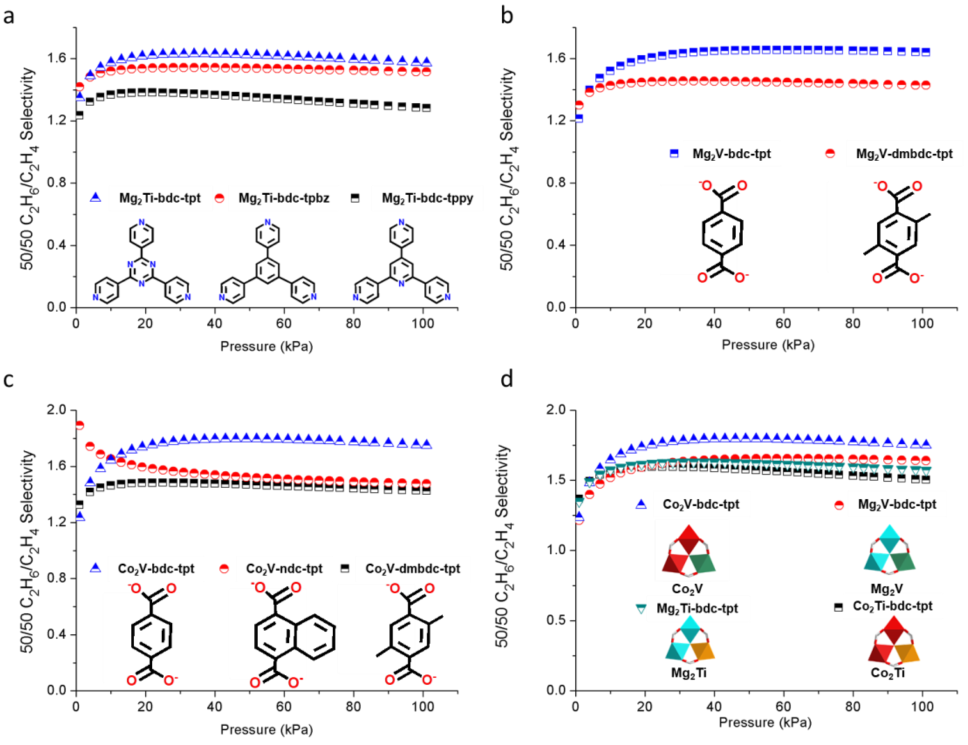

Figure S18. Comparisons of the IAST Selectivities for C_2H_6/C_2H_4 mixture (50/50). a: Selectivities of Mg_2Ti-bdc MOFs with different ligand 2 ; b: Selectivities of Mg_2V-bdc MOFs with different ligand 1; c: Selectivities of Co_2V-tpt MOFs with different ligand 1; d: Selectivities of bdc-tpt MOFs with different metal trimers.

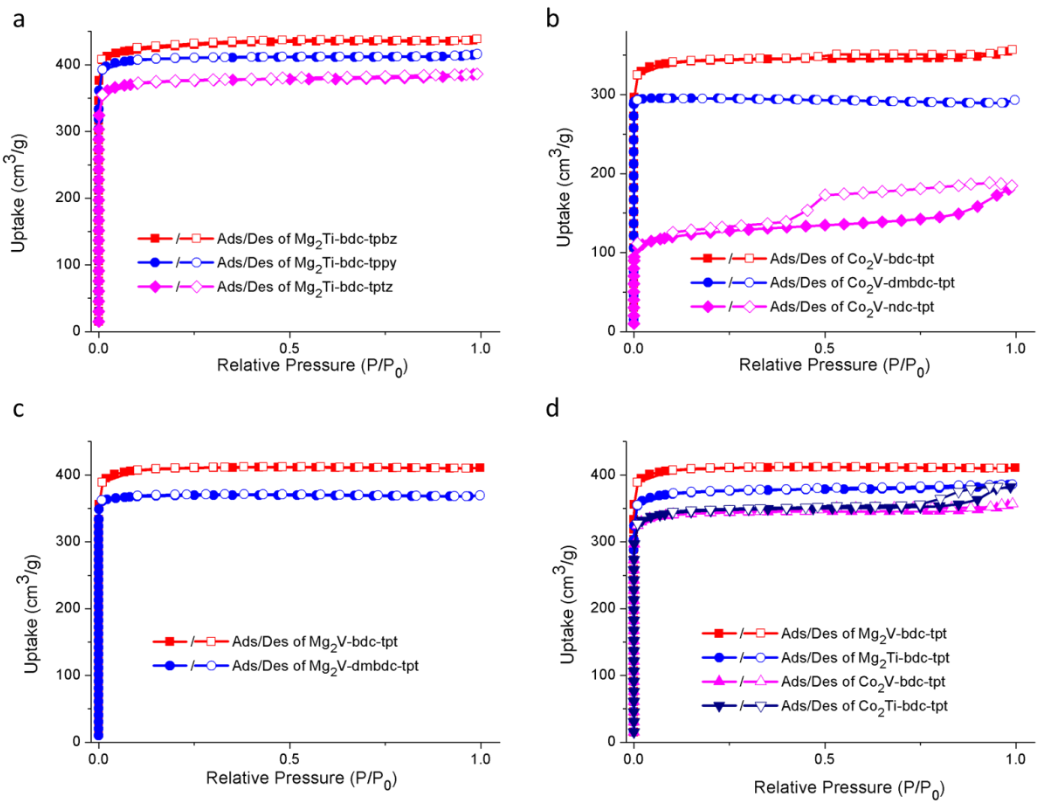

Figure S19. Comparisons of N_2 adsorption at 77 K for all the compounds in this study. a: N_2 adsorption isotherms of Mg_2Ti-bdc MOFs with different ligand 2 ; b: N_2 adsorption isotherms of Mg_2V-bdc MOFs with different ligand 1; c: N_2 adsorption isotherms of Co_2V-tpt MOFs with different ligand 1; d: N_2 adsorption isotherms of bdc-tpt MOFs with different metal trimers. Note that there is significant adsorption hysteresis in CPM-736 (Co_2V-ndc-tpt), which is possibly caused by the defects in the structure due the bulky 1,4-ndc ligand. Similar phenomenon could also be observed in another two 1,4-ndc based *pacs* MOFs (CPM-33d & CPM-236).[S1,7]

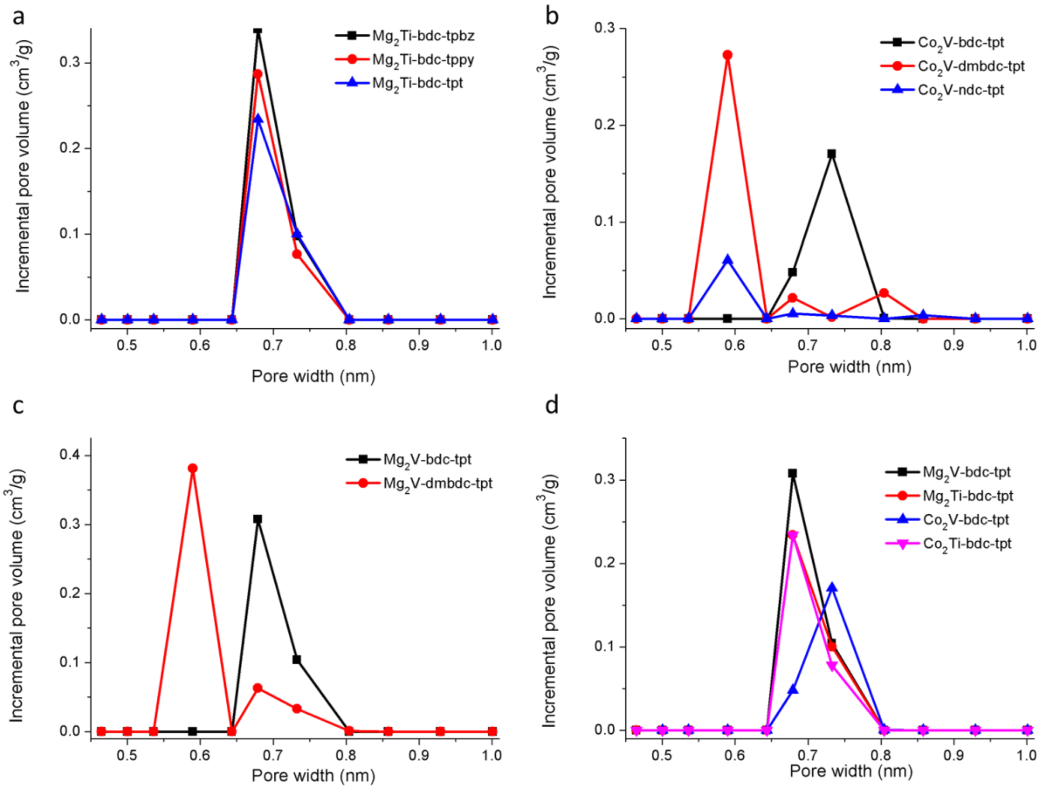

Figure S20. Comparisons of DFT pore size distribution for all the compounds in this study. The pressure range of $P/P_0 < 10^{-3}$ was applied to calculate the pore size due to the micro-porous feature of this family of materials.

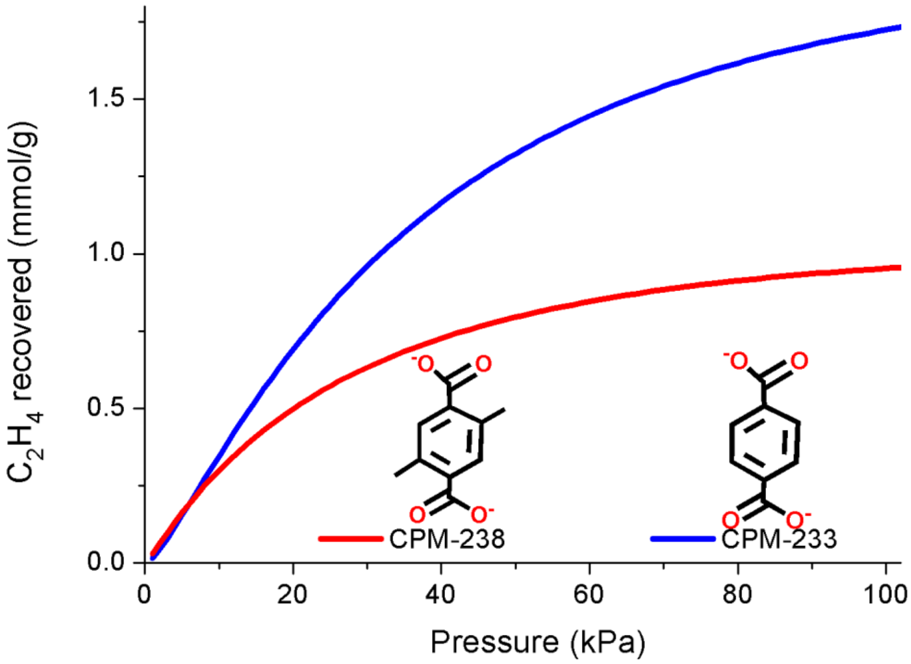

Figure S21. Comparison of separation potential of CPM-233 and CPM-238.

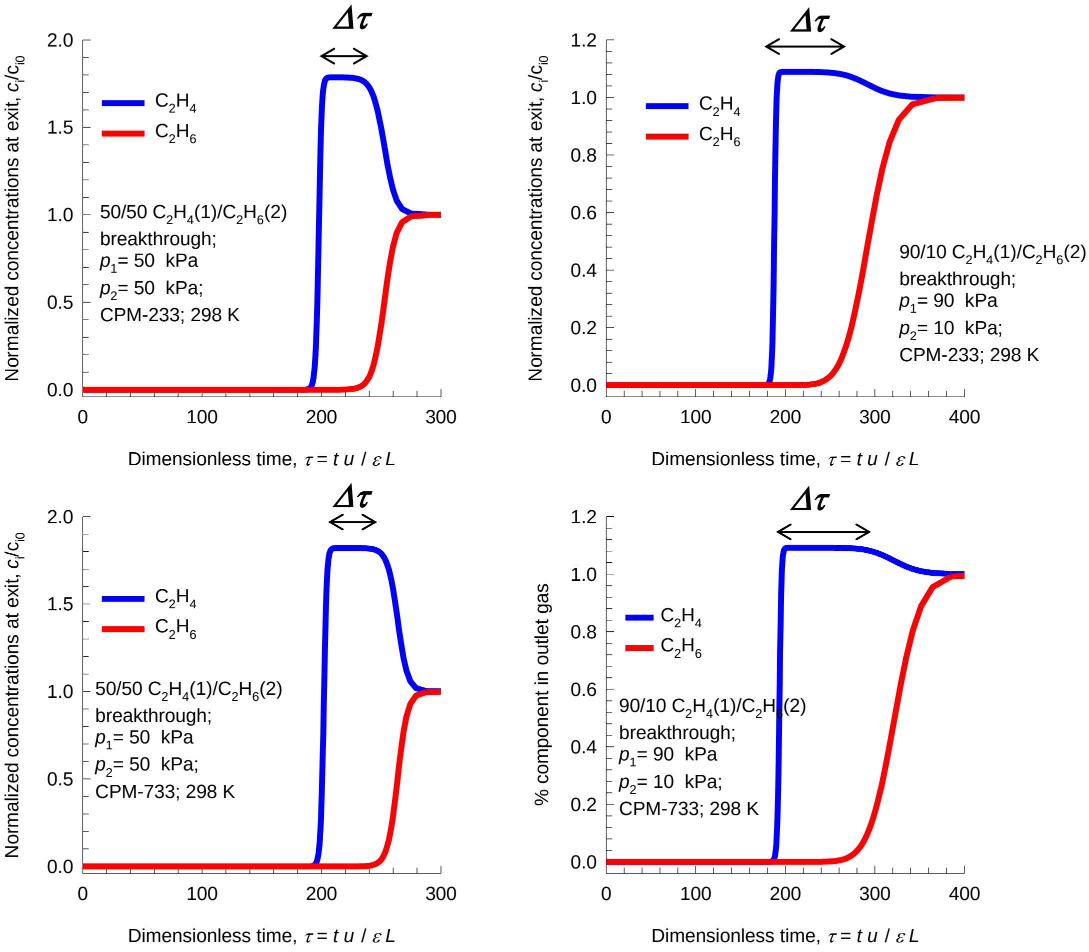

Figure S22. Simulated breakthrough curves for CPM-233 and CPM-723 with 50/50 and 10/90 C_2H_6/C_2H_4 mixture.

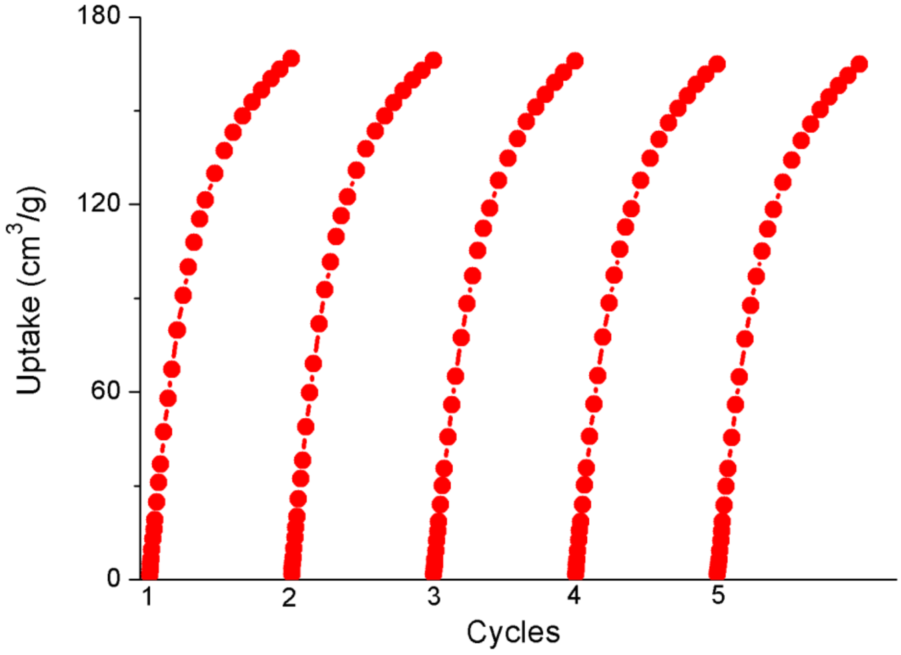

Figure 23. Multiple ethane adsorption test of Mg2V-bdc-tpt at 298 K, showing almost no loss of capacity after 5 cycles.

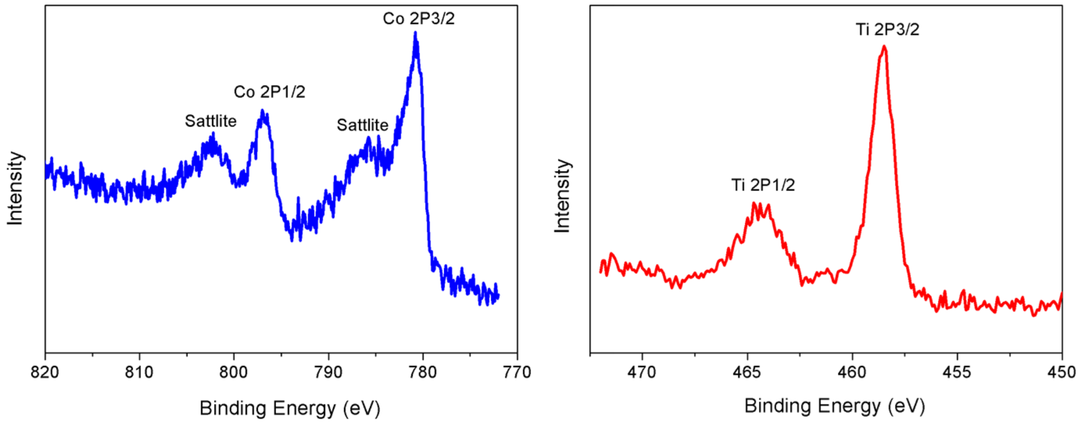

Figure S24. X-ray photoelectron spectroscopy of Co_2Ti-bdc-tpt showing the Co 2p (left) and Ti 2p peaks (right). The satellite peaks shown on Co2p are characteristic of Co^{2+}. Two peaks located at around 464.4 eV and 458.5 eV, correspond to Ti 2p1/2 and Ti 2p3/2 , respectively, indicating an oxidation state of Ti^{4+}.

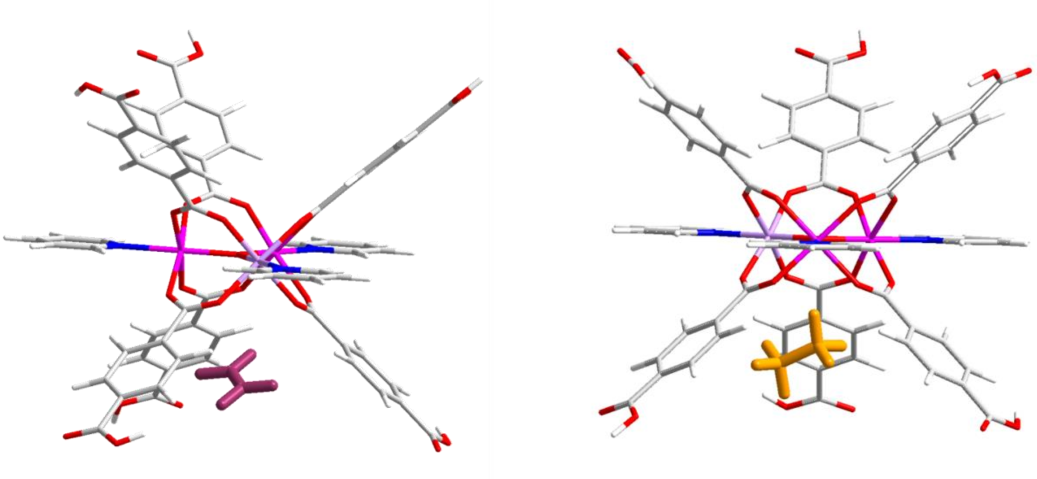

Figure S25. The preferential C_2H_4 and C_2H_6 adsorption sites determined by DFT calculation.

We performed DFT calculations to gain insight into the selective adsorption mechanism. The results indicated that the C_2H_6 binding energy at its most preferred binding site is around −35.85 kJ/mol, higher that that for C_2H_4 (−33.76 kJ/mol). As shown in Figure S25, the gas molecules are trapped in the pocket defined by three phenyl rings via van der Waals interactions between the ethane and the neighboring π electron clouds. For C_2H_6, six hydrogens can interact with the adjacent phenyl rings via C−H···π interaction. In contrast, four hydrogens from C_2H_4 interact with the adjacent phenyl rings. The more interaction points of ethane could account for its higher binding energy.

Table S1. The numbering scheme and names for the MOFs reported in this work

Numbering Code	Metal trimers	Dicarboxylic ligand	Partitioning Ligand	Composition code
CPM-223-tpbz	$(Mg_2Ti)O$	bdc	tpbz	Mg_2Ti-bdc-tpbz
CPM-223-tppy	$(Mg_2Ti)O$	bdc	tppy	Mg_2Ti-bdc-tppy
CPM-223	$(Mg_2Ti)O$	bdc	tpt	Mg_2Ti-bdc-tpt
CPM-233	$(Mg_2V)OH$	bdc	tpt	Mg_2V-bdc-tpt
CPM-238	$(Mg_2V)OH$	dmbdc	tpt	Mg_2V-dmbdc-tpt
CPM-723	$(Co_2Ti)O$	bdc	tpt	Co_2Ti-bdc-tpt
CPM-733	$(Co_2V)OH$	bdc	tpt	Co_2V-bdc-tpt
CPM-736	$(Co_2V)OH$	1,4-ndc	tpt	Co_2V-ndc-tpt
CPM-738	$(Co_2V)OH$	dmbdc	tpt	Co_2V-dmbdc-tpt

Table S2. Summary of gas adsorption properties for MOFs reported in this work

MOFs	BET surface area (m^2/g)	Pore size (Å)	C_2H_6 298K, 1bar (cm^3/g)	C_2H_4 298K, 1bar (cm^3/g)	C_2H_6/C_2H_4 selectivity	Q^0_{st} (C_2H_6) (kJ/mol)	Q^0_{st} (C_2H_4) (kJ/mol)	C_2H_6 273 K, 1bar (cm^3/g)	C_2H_4 273 K, 1bar (cm^3/g)	CO_2 273 K, 1bar (cm^3/g)	CO_2 298 K, 1bar (cm^3/g)
CPM-733 Co_2V-bdc-tpt	1328.5	7.3	159.6	142.7	1.75	23.4	22.5	186.3	190.0	152.5	75.8
CPM-736 Co_2V-ndc-tpt	472.5	5.9	90.2	86.9	1.48	30.4	30.1	108.9	128.9	-	-
CPM-738 Co_2V-dmbdc-tpt	1161.5	5.9	104.6	102.1	1.42	27.9	26.5	131.9	140.2	-	-
CPM-723 Co_2Ti-bdc-tpt	1369.8	6.8	154.7	149.4	1.50	21.7	20.0	187.7	194.9	152.6	76.2
CPM-223 Mg_2Ti-bdc-tpt	1460.6	6.8	54.8	142.1	1.57	25.4	25.0	190.8	200.9	167.4	82.5
CPM-223-tppy Mg_2Ti-bdc-tppy	1599.1	6.8	160.6	164.5	1.28	25.0	22.6	204.0	221.4	182.9	94.8
CPM-223-tpbz Mg_2Ti-bdc-tpbz	1661.7	6.8	154.2	140.0	1.51	21.9	23.3	201.4	197.2	-	-
CPM-233 Mg_2V-bdc-tpt	1597.9	6.8	166.8	146.1	1.64	27.3	26.7	178.6	189.0	179.3	89.3

CPM-238 Mg$_2$V-dmbdc-tpt	1444.4	5.9	124.6	117.6	1.43	24.7	24.4	162.3	172.5	-	-

-: not tested

Table S3. Summary of ethane uptake properties in ethane-selective MOFs (~1 bar and ~ 298 K). 50/50 C_2H_6/C_2H_4 mixture was used in all IAST calculations.

MOFs	C_2H_6 uptake		C_2H_6 uptake in C_2H_6/C_2H_4 mixture (cm³/g)	Separation potential (mmol/g)	Selectivity	Q^0_{st} (C_2H_6) (kJ/mol)	Ref.
	G^a (cm³/g)	V^b (cm³/cm³)					
Mg2V-bdc-tpt	**166.8**	**139.1**	**99.2**	**1.73**	**1.64**	**27.3**	**This work**
Mg2Ti-bdc-tppy	**160.6**	**128.6**	**91.4**	**0.90**	**1.28**	**25.0**	**This work**
Co2V-bdc-tpt	**159.6**	**142.0**	**96.8**	**1.88**	**1.75**	**23.4**	**This work**
Mg2Ti-bdc-tpt	**154.8**	**126.0**	**92.1**	**1.50**	**1.57**	**25.4**	**This work**
Co2Ti-bdc-tpt	**154.7**	**137.5**	**92.2**	**1.38**	**1.50**	**21.0**	**This work**
Mg2Ti-bdc-tpbz	**154.2**	**124.4**	**89.6**	**1.36**	**1.51**	**21.9**	**This work**
Mg2V-dmbdc-tpt	**124.6**	**103.9**	**71.3**	**0.95**	**1.43**	**24.7**	**This work**
PCN-250	116.7	111.7	66.3	1.48	1.9	23.2	S8
Ni(BDC)(TED)0.5	112	114.2	55.6	1.01	1.6	21.5	S9
MUF-15	105.05	131.0	70.1	1.53	1.96c	29.2	S10
Co2V-dmbdc-tpt	**104.6**	**N.A.**	**60.5**	**0.81**	**1.42**	**27.9**	**This work**
IRMOF-8	92	82.4	48.4	1.41	1.6	52.5	S11
Co2V-ndc-tpt	**90.2**	**N.A.**	**52.5**	**0.76**	**1.48**	**30.4**	**This work**

MIL-142A	85.1	75.1	47.0	0.71d	1.51	27.2	S12, S10
TJT-100	82	100.8	49.5	0.73	1.2/1.49c	29	S13
Fe2(O2)(DOBDC)	74.3	93.2	56.7	1.93	4.4	66.8	S14
PCN-245	73.2	52.6	40.3	0.80e	1.8	22.8	S15, S10
ZIF-8	45.4	48.4	28.2	0.56b	1.8	17.2	S16, S10
ZIF-4	51.5	66.8	34.9	0.83b	2.15	N.A.	S17, S10
Cu(Qc)2	41.5	60.0	37.0	0.85	3.41	30	S18
ZIF-7	41.1	51.0	26.9	0.94b	1.5	N.A.	S19, S10
MAF-49	38.8	57.5	27.1	0.78	2.71	61	S20, S14

[a] Gravimetric uptake. [b] Volumetric uptake. [c] The IAST-calculated selectivity of 1.79 was obtained in this work as compared to the value of 1.96 from ref. S8. [d] The calculation of separation potential for MIL-142A, PCN-245, ZIF-8, and ZIF-4, and ZIF-7 are from Table S5 of ref. S8. [e] The value reported in the ref. S11 is 1.2.

N.A.: not available.

Table S4. Summary of MOFs with high ethane uptake at ~1 bar and around room temperature. Both ethane-selective MOFs and ethylene selective MOFs are included.

MOFs	C_2H_6 uptake (cm³/g)	Ethane or Ethylene selective	temperature	Ref.
Mg2V-bdc-tpt	166.8	**Ethane**	298	**This work**
NOTT-101	163	Ethylene	296 K	S21
Mg2Ti-bdc-tppy	**160.6**	**Ethane**	**298 K**	**This work**
Co2V-bdc-tpt	**159.6**	**Ethane**	**298 K**	**This work**
PCN-16	155	Ethylene	**296**	S21
CoTi-bdc-tpt	**154.7**	**Ethane**	**298 K**	**This work**
Cu-TDPAT	154.4	Ethylene	298 K	S22
MgTi-bdc-tpbz	**154.2**	**Ethane**	**298 K**	**This work**
ZJU-11a	154	Ethylene	298 K	S23
Mg-MOF-74	144	Ethylene	296 K	S21
Co-MOF-74	142/145	Ethylene	298 K	S24, S21
HKUST-1	138	Ethylene	296 K	S21
ZJU-60a	136.7	Ethylene	296 K	S25
MOF-505	125	Ethylene	296	S21
Ni-MOF-74	121	Ethylene	298 K	S24

PCN-250	116.70	**Ethane**	298 K	S8
UMCM-150	113	Ethylene	296 K	S21
Ni(BDC)(TED)0.5	112	**Ethane**	298 K	S9
Cu-TDPAH	107.2	Ethylene	298 K	S26
MUF-15	105.05	**Ethane**	293 K	S10

Table S5. Summary of the refined parameters with Single-Site Langmuir-Freundlich fitting for the pure adsorption isotherms of C_2H_4 and C_2H_6.

MOFs	Gases	N_{sat}(mmol·g^{-1})	b (kPa$^{-1/n}$)	1/n	R^2
CPM-733	C_2H_4	11.19137	0.01345	0.99567	0.99979
Co_2V-bdc-tpt	C_2H_6	8.52615	0.02551	1.14363	0.99993
CPM-736	C_2H_4	5.06259	0.04101	0.9439	0.99991
Co_2V-ndc-tpt	C_2H_6	4.92313	0.07117	0.8874	0.99963
CPM-738	C_2H_4	6.31334	0.02611	0.99322	0.99996
Co_2V-dmbdc-tpt	C_2H_6	5.49793	0.04235	1.0489	0.99986
CPM-723	C_2H_4	10.74372	0.01265	1.05384	0.99995
Co_2Ti-bdc-tpt	C_2H_6	8.43098	0.02436	1.12965	0.99994
CPM-223-tpbz	C_2H_4	9.49258	0.01066	1.12633	0.99991
MgTi-bdc-tpb	C_2H_6	8.62664	0.01813	1.16498	0.99993
CPM-223-tppy	C_2H_4	11.62725	0.01191	1.07594	0.99999
Mg_2Ti-bdc-tpp	C_2H_6	8.99423	0.02059	1.13631	0.99996
CPM-223	C_2H_4	11.03222	0.01182	1.02759	0.99997
Mg_2Ti-bdc-tpt	C_2H_6	8.76043	0.02217	1.10939	0.99996
CPM-233	C_2H_4	11.22692	0.01234	1.02397	0.99995
Mg_2V-bdc-tpt	C_2H_6	9.33279	0.02041	1.13942	0.99994
CPM-238	C_2H_4	7.85891	0.02556	0.94192	0.99992
Mg_2V-dmbdc-tpt	C_2H_6	7.00888	0.03889	0.98914	0.99990

Table S6. Crystal data and structure refinement for CPM-723 (Co_2Ti-bdc-tpt).

Identification code	Co2Ti-bdc-tpt	
Empirical formula	C42 H24 Co2.06 N6 O13 Ti0.94	
Formula weight	987.09	
Temperature	296(2) K	
Wavelength	0.71073 Å	
Crystal system	Hexagonal	
Space group	$P6_3/mmc$	
Unit cell dimensions	a = 16.871(3) Å	α= 90°.
	b = 16.871(3) Å	β= 90°.
	c = 14.955(2) Å	γ = 120°.
Volume	3686.3(12) $Å^3$	
Z	2	
Density (calculated)	0.889 Mg/m^3	
Absorption coefficient	0.599 mm^{-1}	
F(000)	997	
Theta range for data collection	1.949 to 23.254°.	
Index ranges	-18<=h<=18, -18<=k<=18, -16<=l<=16	
Reflections collected	19495	
Independent reflections	1037 [R(int) = 0.0842]	
Completeness to theta = 23.254°	99.8 %	
Refinement method	Full-matrix least-squares on F^2	
Data / restraints / parameters	1037 / 0 / 66	
Goodness-of-fit on F^2	1.170	
Final R indices [I>2sigma(I)]	R1 = 0.0338, wR2 = 0.1439	
R indices (all data)	R1 = 0.0427, wR2 = 0.1493	
Largest diff. peak and hole	0.231 and -0.440 e.$Å^{-3}$	

Table S7. Crystal data and structure refinement for CPM-733 (Co$_2$V-bdc-tpt).

Identification code	Co2V-bdc-tpt	
Empirical formula	C42 H24 Co2 N6 O13 V	
Formula weight	989.47	
Temperature	296(2) K	
Wavelength	0.71073 Å	
Crystal system	Hexagonal	
Space group	P6$_3$/mmc	
Unit cell dimensions	a = 16.89(2) Å	α= 90°.
	b = 16.89(2) Å	β= 90°.
	c = 14.94(2) Å	γ = 120°.
Volume	3693(12) Å^3	
Z	2	
Density (calculated)	0.890 Mg/m^3	
Absorption coefficient	0.610 mm^{-1}	
F(000)	998	
Theta range for data collection	1.948 to 19.987°.	
Index ranges	-16<=h<=16, -16<=k<=12, -14<=l<=8	
Reflections collected	6635	
Independent reflections	689 [R(int) = 0.1567]	
Completeness to theta = 19.987°	99.6 %	
Refinement method	Full-matrix least-squares on F^2	
Data / restraints / parameters	689 / 0 / 65	
Goodness-of-fit on F^2	1.042	
Final R indices [I>2sigma(I)]	R1 = 0.0443, wR2 = 0.1094	
R indices (all data)	R1 = 0.0634, wR2 = 0.1140	
Largest diff. peak and hole	0.294 and -0.349 e.Å^{-3}	

Table S8. Crystal data and structure refinement for CPM-223 (Mg$_2$Ti-bdc-tpt).

Identification code	Mg2Ti-bdc-tpt	
Empirical formula	C42 H24 Mg2.22 N6 O13 Ti0.78	
Formula weight	912.00	
Temperature	296(2) K	
Wavelength	0.71073 Å	
Crystal system	Hexagonal	
Space group	$P6_3/mmc$	
Unit cell dimensions	a = 17.014(12) Å	a= 90°.
	b = 17.014(12) Å	b= 90°.
	c = 14.838(10) Å	g = 120°.
Volume	3720(6) Å^3	
Z	2	
Density (calculated)	0.814 Mg/m^3	
Absorption coefficient	0.154 mm^{-1}	
F(000)	932	
Theta range for data collection	1.948 to 25.458°.	
Index ranges	-20<=h<=20, -20<=k<=20, -13<=l<=17	
Reflections collected	17564	
Independent reflections	1324 [R(int) = 0.0686]	
Completeness to theta = 25.242°	99.9 %	
Refinement method	Full-matrix least-squares on F^2	
Data / restraints / parameters	1324 / 0 / 66	
Goodness-of-fit on F^2	0.997	
Final R indices [I>2sigma(I)]	R1 = 0.0338, wR2 = 0.1301	
R indices (all data)	R1 = 0.0425, wR2 = 0.1354	
Largest diff. peak and hole	0.195 and -0.267 e.Å^{-3}	

Table S9. Crystal data and structure refinement for CPM-223-tpbz (Mg_2Ti-bdc-tpbz).

Identification code	Mg2Ti-bdc-tpbz.	
Empirical formula	C45 H27 Mg2.25 N3 O13 Ti0.75	
Formula weight	908.43	
Temperature	296(2) K	
Wavelength	0.71073 Å	
Crystal system	Hexagonal	
Space group	$P6_3/mmc$	
Unit cell dimensions	a = 17.234(4) Å	a= 90°.
	b = 17.234(4) Å	b= 90°.
	c = 14.537(3) Å	g = 120°.
Volume	3739.2(19) $Å^3$	
Z	2	
Density (calculated)	0.807 Mg/m^3	
Absorption coefficient	0.149 mm^{-1}	
F(000)	931	
Theta range for data collection	1.364 to 25.327°.	
Index ranges	-20<=h<=20, -20<=k<=19, -17<=l<=17	
Reflections collected	20380	
Independent reflections	1319 [R(int) = 0.0823]	
Completeness to theta = 25.242°	100.0 %	
Refinement method	Full-matrix least-squares on F^2	
Data / restraints / parameters	1319 / 0 / 66	
Goodness-of-fit on F^2	1.062	
Final R indices [I>2sigma(I)]	R1 = 0.0405, wR2 = 0.1509	
R indices (all data)	R1 = 0.0571, wR2 = 0.1602	
Largest diff. peak and hole	0.299 and -0.346 e.$Å^{-3}$	

Table S10. Crystal data and structure refinement for CPM-223-tppy (Mg_2Ti-bdc-tppy).

Identification code	Mg2Ti-bdc-tppy	
Empirical formula	C44 H26 Mg2.16 N4 O13 Ti0.84	
Formula weight	911.43	
Temperature	296(2) K	
Wavelength	0.71073 Å	
Crystal system	Hexagonal	
Space group	$P6_3/mmc$	
Unit cell dimensions	a = 17.20(3) Å	α= 90°.
	b = 17.20(3) Å	β= 90°.
	c = 14.75(3) Å	γ = 120°.
Volume	3778(17) Å^3	
Z	2	
Density (calculated)	0.801 Mg/m^3	
Absorption coefficient	0.156 mm^{-1}	
F(000)	933	
Theta range for data collection	1.943 to 23.215°.	
Index ranges	-18<=h<=17, -17<=k<=19, -16<=l<=16	
Reflections collected	14680	
Independent reflections	1044 [R(int) = 0.0782]	
Completeness to theta = 23.215°	98.9 %	
Refinement method	Full-matrix least-squares on F^2	
Data / restraints / parameters	1044 / 0 / 66	
Goodness-of-fit on F^2	1.083	
Final R indices [I>2sigma(I)]	R1 = 0.0397, wR2 = 0.1173	
R indices (all data)	R1 = 0.0542, wR2 = 0.1267	
Largest diff. peak and hole	0.167 and -0.358 e.Å^{-3}	

Table S11. Crystal data and structure refinement for CPM-233 (Mg_2V-bdc-tpt).

Identification code	Mg2V-bdc-tpt	
Empirical formula	C42 H24 Mg2 N6 O13 V	
Formula weight	920.23	
Temperature	296(2) K	
Wavelength	0.71073 Å	
Crystal system	Hexagonal	
Space group	$P6_3/mmc$	
Unit cell dimensions	a = 16.985(15) Å	α= 90°.
	b = 16.985(15) Å	β= 90°.
	c = 14.669(13) Å	γ = 120°.
Volume	3665(7) $Å^3$	
Z	2	
Density (calculated)	0.834 Mg/m^3	
Absorption coefficient	0.195 mm^{-1}	
F(000)	938	
Theta range for data collection	1.961 to 23.410°.	
Index ranges	-10<=h<=18, -18<=k<=18, -16<=l<=16	
Reflections collected	11227	
Independent reflections	1032 [R(int) = 0.0808]	
Completeness to theta = 23.410°	98.4 %	
Refinement method	Full-matrix least-squares on F^2	
Data / restraints / parameters	1032 / 0 / 66	
Goodness-of-fit on F^2	1.164	
Final R indices [I>2sigma(I)]	R1 = 0.0381, wR2 = 0.1284	
R indices (all data)	R1 = 0.0500, wR2 = 0.1321	
Largest diff. peak and hole	0.226 and -0.307 e.$Å^{-3}$	

Table S12. Crystal data and structure refinement for CPM-238 (Mg$_2$V-dmbdc-tpt).

Identification code	Mg2V-dmbdc-tpt	
Empirical formula	C48 H30 Mg1.92 N6 O13 V1.08	
Formula weight	1000.47	
Temperature	296(2) K	
Wavelength	0.71073 Å	
Crystal system	Hexagonal	
Space group	P6$_3$/mmc	
Unit cell dimensions	a = 16.79(4) Å	α= 90°.
	b = 16.79(4) Å	β= 90°.
	c = 14.84(4) Å	γ = 120°.
Volume	3622(21) Å^3	
Z	2	
Density (calculated)	0.917 Mg/m^3	
Absorption coefficient	0.210 mm^{-1}	
F(000)	1024	
Theta range for data collection	1.401 to 20.845°.	
Index ranges	-9<=h<=16, -16<=k<=9, -12<=l<=10	
Reflections collected	5730	
Independent reflections	727 [R(int) = 0.1071]	
Completeness to theta = 20.845°	95.4 %	
Refinement method	Full-matrix least-squares on F^2	
Data / restraints / parameters	727 / 6 / 75	
Goodness-of-fit on F^2	1.187	
Final R indices [I>2sigma(I)]	R1 = 0.0675, wR2 = 0.1759	
R indices (all data)	R1 = 0.0991, wR2 = 0.1904	
Largest diff. peak and hole	0.305 and -0.252 e.Å^{-3}	

Reference

S1. Zhai, Q.-G.; Bu, X.; Mao, C.; Zhao, X.; Daemen, L.; Cheng, Y.; Ramirez-Cuesta, A. J.; Feng, P. An ultra-tunable platform for molecular engineering of high-performance crystalline porous materials. *Nat. Comm.* **2016**, *7*, 13645.

S2. Myers, A. L.; Prausnitz, J. M. Thermodynamics of mixed-gas adsorption. *AlChE J.* **1965**, *11*, 121.

S3. Krishna, R. Screening metal–organic frameworks for mixture separations in fixed-bed adsorbers using a combined selectivity/capacity metric. *RSC Advances* **2017**, *7*, 35724.

S4. Delley, B. From molecules to solids with the DMol3 approach. *J. Chem. Phys.* **2000**, *113*, 7756.

S5. Grimme, S. Semiempirical GGA-type density functional constructed with a long-range dispersion correction. *J. Comput. Chem.* **2006**, *27*, 1787.

S6. Krishna, R. Methodologies for evaluation of metal–organic frameworks in separation applications. *RSC Advances* **2015**, *5*, 52269.

S7. Zhao, X.; Bu, X.; Zhai, Q.-G.; Tran, H.; Feng, P. Pore Space Partition by Symmetry-Matching Regulated Ligand Insertion and Dramatic Tuning on Carbon Dioxide Uptake. *J. Am. Chem. Soc.* **2015**, *137*, 1396.

S8. Chen, Y.; Qiao, Z.; Wu, H.; Lv, D.; Shi, R.; Xia, Q.; Zhou, J.; Li, Z. An ethane-trapping MOF PCN-250 for highly selective adsorption of ethane over ethylene. *Chem. Eng. Sci.* **2018**, *175*, 110.

S9. Liang, W.; Xu, F.; Zhou, X.; Xiao, J.; Xia, Q.; Li, Y.; Li, Z. Ethane selective adsorbent Ni(bdc)(ted)0.5 with high uptake and its significance in adsorption separation of ethane and ethylene. *Chem. Eng. Sci.* **2016**, *148*, 275.

S10. Qazvini, O. T.; Babarao, R.; Shi, Z.-L.; Zhang, Y.-B.; Telfer, S. G. A Robust Ethane-Trapping Metal–Organic Framework with a High Capacity for Ethylene Purification. *J. Am. Chem. Soc.* **2019**, *141*, 5014.

S11. Pires, J.; Pinto, M. L.; Saini, V. K. Ethane Selective IRMOF-8 and Its Significance in Ethane–Ethylene Separation by Adsorption. *ACS Appl. Mater. Inter.* **2014**, *6*, 12093.

S12. Chen, Y.; Wu, H.; Lv, D.; Shi, R.; Chen, Y.; Xia, Q.; Li, Z. Highly Adsorptive Separation of Ethane/Ethylene by An Ethane-Selective MOF MIL-142A. *Industrial & Engineering Chemistry Research* **2018**, *57*, 4063.

S13. Hao, H.-G.; Zhao, Y.-F.; Chen, D.-M.; Yu, J.-M.; Tan, K.; Ma, S.; Chabal, Y.; Zhang, Z.-M.; Dou, J.-M.; Xiao, Z.-H.; Day, G.; Zhou, H.-C.; Lu, T.-B. Simultaneous Trapping of C_2H_2 and C_2H_6 from a Ternary Mixture of $C_2H_2/C_2H_4/C_2H_6$ in a Robust Metal–Organic Framework for the Purification of C_2H_4. *Angew. Chem.* **2018**, *130*, 16299.

S14. Li, L.; Lin, R.-B.; Krishna, R.; Li, H.; Xiang, S.; Wu, H.; Li, J.; Zhou, W.; Chen, B. Ethane/ethylene separation in a metal-organic framework with iron-peroxo sites. *Science* **2018**, *362*, 443.

S15. Lv, D.; Shi, R.; Chen, Y.; Wu, Y.; Wu, H.; Xi, H.; Xia, Q.; Li, Z. Selective Adsorption of Ethane over Ethylene in PCN-245: Impacts of Interpenetrated Adsorbent. *ACS Appl. Mater. Inter.* **2018**, *10*, 8366.

S16. Böhme, U.; Barth, B.; Paula, C.; Kuhnt, A.; Schwieger, W.; Mundstock, A.; Caro, J.; Hartmann, M. Ethene/Ethane and Propene/Propane Separation via the Olefin and Paraffin Selective Metal–Organic Framework Adsorbents CPO-27 and ZIF-8. *Langmuir* **2013**, *29*, 8592.

S17. Hartmann, M.; Böhme, U.; Hovestadt, M.; Paula, C. Adsorptive Separation of Olefin/Paraffin Mixtures with ZIF-4. *Langmuir* **2015**, *31*, 12382.

S18. Lin, R.-B.; Wu, H.; Li, L.; Tang, X.-L.; Li, Z.; Gao, J.; Cui, H.; Zhou, W.; Chen, B. Boosting Ethane/Ethylene Separation within Isoreticular Ultramicroporous Metal–Organic Frameworks. *J. Am. Chem. Soc.* **2018**, *140*, 12940.

S19. Gücüyener, C.; van den Bergh, J.; Gascon, J.; Kapteijn, F. Ethane/Ethene Separation Turned on Its Head: Selective Ethane Adsorption on the Metal−Organic Framework ZIF-7 through a Gate-Opening Mechanism. *J. Am. Chem. Soc.* **2010**, *132*, 17704.

S20. Liao, P.-Q.; Zhang, W.-X.; Zhang, J.-P.; Chen, X.-M. Efficient purification of ethene by an ethane-trapping metal-organic framework. *Nat. Comm.* **2015**, *6*, 8697.

S21. He, Y.; Krishna, R.; Chen, B. Metal–organic frameworks with potential for energy-efficient adsorptive separation of light hydrocarbons. *Energy & Environmental Science* **2012**, *5*, 9107.

S22. Liu, K.; Ma, D.; Li, B.; Li, Y.; Yao, K.; Zhang, Z.; Han, Y.; Shi, Z. High storage capacity and separation selectivity for C2 hydrocarbons over methane in the metal–organic framework Cu–TDPAT. *J. Mater. Chem. A* **2014**, *2*, 15823.

S23. Duan, X.; Wang, H.; Ji, Z.; Cui, Y.; Yang, Y.; Qian, G. A novel NbO-type metal-organic framework for highly separation of methane from C2-hydrocarbon at room temperature. *Mater. Lett.* **2017**, *196*, 112.

S24. Matzger, A. J.; Wong-Foy, A. G.; Caskey, S.; Google Patents: 2013.

S25. Duan, X.; Zhang, Q.; Cai, J.; Yang, Y.; Cui, Y.; He, Y.; Wu, C.; Krishna, R.; Chen, B.; Qian, G. A new metal–organic framework with potential for adsorptive separation of methane from carbon dioxide, acetylene, ethylene, and ethane established by simulated breakthrough experiments. *J. Mater. Chem. A* **2014**, *2*, 2628.

S26. Liu, K.; Li, B.; Li, Y.; Li, X.; Yang, F.; Zeng, G.; Peng, Y.; Zhang, Z.; Li, G.; Shi, Z.; Feng, S.; Song, D. An N-rich metal–organic framework with an rht topology: high CO2 and C2 hydrocarbons uptake and selective capture from CH4. *Chem. Commun.* **2014**, *50*, 5031.